Arabian Journal for Science and Engineering (2023) 48:3537–3557
https://doi.org/10.1007/s13369-022-07151-3

RESEARCH ARTICLE-MECHANICAL ENGINEERING

Numerical Modeming, Energy–Exergy Analyses, and Multi-objective Programming of the Solar-assisted Heat Pump System Using Genetic Algorithm Coupled with the Multi-criteria Decision Analysis

Masoud Nasouri[1] · **Navid Delgarm**[2]

Received: 21 March 2022 / Accepted: 19 July 2022 / Published online: 6 September 2022

Abstract
In this paper, the numerical modeling of an indirect-expansion solar-assisted heat pump (IDX-SAHP) water heater system is proposed and the exergy-energy analyses and multiple-objective optimization (MOO) of the developed system are investigated. After the verification of the IDX-SAHP with the experimental results, the system performance is examined under the temperate climate of Iran throughout the year. Next, the sensitivity analysis (SA) of diverse variables comprising ambient temperature (T_a), solar intensity (I_T), water temperature at the condenser outlet ($T_{W,o}$), compressor speed (ω), collector area (A_{cl}), thermal conductivity of the collector plate (k_p), number of the glass cover (N_{gl}), tube diameter in the solar collector (D_{cl}), tube length in the condenser (L_{cond}), and absorber thickness of the collector plate (δ) is implemented via the one-parameter-at-a-time (OPAT) technique. Then, the influence of various factors such as T_a, I_T, A_{cl} and ω on the exergy efficiency and exergy destruction of the IDX-SAHP system are studied. Besides, the single-objective optimizations (SOOs) and MOO processes are implemented through Elitist Non-dominated Sorting Genetic Algorithm (NSGA-II) to maximize the coefficient of performance (COP) and the collector efficiency (CE), individually and simultaneously. The results achieved by the SOOs depict that the design of IDX-SAHP as per the COP-based SOO offers a better system compared to the CE-based SOO. Furthermore, the optimal solutions obtained by the MOO are presented in the form of the Prato curve to depict the COP and CE interactions. Afterward, to achieve the final optimum layout of the system, the Analytic Hierarchy Process (AHP) technique as a robust multi-criteria decision analysis method (MCDM) is integrated with the MOO process through MATLAB programming language. The optimization results demonstrate that the MOO process gives better performance compared to the SOO process in such a way that although the CE of the maximized IDX-SAHP reduces a little from 52 to 47%, its COP is enhanced greatly from 3 to 7, resulting in reduction of the total working hour of the system up to 282 hours compared to the initial system, and consequently, the overall power use of the maximized system largely reduces. This investigation clarifies the importance of exergy-energy analyses, SA, MOO, and MCDM during the IDX-SAHP design to increase efficiency and decrease the power use of the system by opting the most appropriate design parameters of the system.

Keywords Solar-assisted heat pump · Performance analysis · Parametric study · Multi-objective optimization · Genetic algorithm · Multi-criteria decision analysis

Abbreviations

A	Area (m^2)
AHP	Analytic Hierarchy Process
ANN	Artificial Neural Network
CE	Collector Efficiency
CI	Consistency Index
COP	Coefficient of Performance
CR	Consistency Ratio
C_p	Specific heat capacity (J/kg·K)
D	Diameter (m)

✉ Masoud Nasouri
M.Nasouri@ut.ac.ir

✉ Navid Delgarm
navid.delgarm@ut.ac.ir

[1] Department of Environment, Aras International Campus, University of Tehran, Tehran 5441656498, Iran

[2] Department of Mechanical and Aerospace Engineering, Malek-Ashtar University of Technology, Isfahan 83145/115, Iran

DHW	Domestic Hot Water
DX-SAHP	Direct Solar Assisted Heat Pump
EES	Energy Equation Solver
E_χ	Exergy
F	Absorber fin efficiency
$F^{'}$	Collector efficiency factor
GWS	Glycol-water solution
h	Specific enthalpy (J/kg)
I_T	Solar intensity (W/m^2)
IDX-SAHP	Indirect—Expansion Solar—Assisted Heat Pump
K	Thermal conductivity (W/m·K)
kW	Kilowatts
L	Length (m)
M	Mass (kg)
MCDA	Multi-Criteria Decision Analysis
MOO	Multiple-objective optimization
MSHs	Monthly Sunshine Hours
$\dot{m}$	Mass flow rate (kg/s)
N	Number of glass cover
NSGA-II	Non-dominated Sorting Genetic Algorithm
O&M	Operation and Maintenance
OPAT	One-Parameter-at-a-Time
PCM	Phase-Change Material
PV/T	Photovoltaic/Thermal
$\dot{Q}^{\cdot}$	Thermal heat rate (W)
RI	Average random consistence indicator of the judgment matrix
S	Solar radiation absorbed by the collector per unit area (W/m^2)
SA	Sensitivity analysi
SAHP	Solar-Assisted Heat Pump
SOO	Single-objective optimization
T	Mean temperature (K)
TEV	Thermostatic Expansion Valve
t	Time (s)
U_L	overall heat loss coefficient (W/m^2·K)
u	Speed (m/s)
V	Volume (m^3)
V_d	Displacement volume rate (m^3/rev)
v	Specific volume (m^3/kg)
W	Pitch of the tube in collector plate (m)
$\dot{W}$	Electrical power consumption

Greek Symbols

α	Absorptivity
β	Collector tilt angle (deg)
δ	Thickness (m)
ε	Emissivity
η	Efficiency
k	Polytropic index
λ	Eigenvalue
μ	Viscosity (Pa·s)
σ	Stefan-Boltzmann constant (W/m^2·K^4)
τ	Transmittance
ψ	Specific stream exergy
ω	Compressor speed (rpm)

Subscripts

a	Ambient air
cond	Condenser
cl	Collector
cm	Compressor
eva	Evaporator
g	Vapor
gl	Glass
gw	Glycol-water
i	Input,inlet
l	Liquid
m	Mean
max	Maximum
o	Output, outlet
p	Plate
r	Refrigerant
rad	Radiation
s	Surface
W	Water
w	Wind

1 Introduction

Iran's geography and climate are highly suitable for solar energy-based technologies. Solar energy can play an important role in Iran's energy security and help to reduce greenhouse gas emissions and fossil fuel use, which is the largest source of Iran's carbon dioxide emissions. In this context, combining solar collectors with the heat pumps in a single combined system, known as the solar-assisted heat pumps (SAHPs), have been developed rapidly during the last decade. SAHPs use solar radiation and ambient energy as the heating source, which can be considered 'free' energy [1, 2]. In a SAHP system, the solar thermal panels act as a low-temperature heat source and the produced heat is utilized to feed the evaporator of the heat pump [3]. The aim of SAHPs design is to produce energy more efficiently and less expensively to reach a high COP. SAHPs are widely used for producing domestic hot water (DHW) and can efficiently serve up to 80% of hot water needs with no fuel cost or pollution and with minimal operation and

maintenance (O&M) expense [4]. SAHPs may be categorized into two types such as direct solar-assisted heat pump (DX-SAHP) and indirect solar-assisted heat pump (IDX-SAHP) [5]. In recent years, several researches have been conducted on the DX-SAHPs and IDX-SAHPs. Shi et al. [3] presented the advancements and the current status of DX-SAHPs. Further, Cao et al. [6] simulated a thermodynamic model of a DX-SAHP and optimized its performance. Newly, Song et al. [7] proposed a novel DX-SAHP with a hybrid compound parabolic concentrator/photovoltaic/fin evaporator to make full use of solar and air energy in a limited space. Mohanraj et al. [8] experimentally analyzed the economic of a heat pump water heater-assisted regenerative solar still using latent heat storage. Moreover, Duarte et al. [9] carried out an experimental analysis of the influence of environmental conditions in a small size DX-SAHP operating with CO_2 as the refrigerant to heat water. Singh et al. [10] designed, built, and experimentally studied a convective closed-loop SAHP for both simple heat pump drying and SAHP drying modes. In another research, Kong et al. [11] examined the efficiency of a DX-SAHP using R290 with micro-channel heat transfer technology during the winter period, experimentally. Belmonte et al. [12] simulated two different SAHPs able to cover a significant part of the space heating demand of a single-family house located in Madrid (Spain) using TRNSYS. Besides, Sezen et al. [13] investigated the effect of ambient conditions on heating modes, and identify the preferable ambient condition ranges for each SAHP system depends on their heating modes. Song et al. [14] analyzed the optimal structure of evaporator, three direct-expansion solar-assisted heat pumps with Fresnel PV evaporator (FPV-SAHP), hybrid Fresnel PV plus thermoelectric generator (TEG) evaporator (FPV/TEG-SAHP), and traditional PV evaporator (PV-SAHP). Singh et al. [15] developed a batch-type solar-assisted heat pump dryer (SAHPD) and experimented in both simple heat pump dryer (HPD) and SAHPD modes for closed system drying of banana chips. Furthermore, Simonetti et al. [16] presented a yearly energetic and economic assessment of three different solar-assisted heat pump concepts integrated with electrical and thermal storages and applied to a single-family house. Recently, Chen et al. [17] presented a continuing research on the direct expansion solar-assisted ejector-compression heat pump cycle for water heater aiming to reveal the system dynamic characteristic by experimental method. Yang et al. [18] modeled the serial, parallel, and dual-source indirect expansion solar-assisted air source heat pumps and simulated under the weather conditions in London using TRNSYS to investigate the operating performance over a typical year. Additionally, Li and Mao [19] utilized TRNSYS to optimize the solar thermal and heat pump combisystems under five distinct climatic conditions. Zhou et al. [20] presented the investigation of a novel mini channel Photovoltaic/Thermal (PV/T) combined heat pump system using both experimental and theoretical methods. Kim et al. [21] carried out a comparative investigation of various IDX-SAHPs. Recently, Huan et al. [22] simulated an IDX-SAHP using TRNSYS for a university bathroom in Xi'an and validated it through experimental measurements. Ma et al. [23] conducted the performance analysis of an IDX-SAHP with CO_2 refrigerant. Singh et al. [24] performed an experimental performance analysis of an IDX-SAHP dryer for banana chips. Also, Liu et al. [25] developed a novel low-concentrating photovoltaic/thermal solar-assisted water source heat pump (LCPV/T-WWHP) system to satisfy both electricity and thermal demand of a university building. Youssef et al. [4, 26] experimentally studied an IDX-SAHP with latent heat storage. Bridgeman et al. [27] constructed an IDX-SAHP with the glycol–water solution (GWS) in the collector loop and verified the obtained experimental results with the results of the investigation conducted by Freeman et al. [28]. Besides, Oztop et al. [29] reviewed the previously conducted studies and applications in terms of design, performance assessment, heat transfer enhancement techniques, experimental and numerical works, thermal heat storage, effectiveness compassion and recent advances. In another work, Bayrak et al. [30] assessed and compared the performance of five types of solar air heaters and determined the energy and exergy efficiencies. Also, Zhang et al. [31] presented an auspicious method, the multi-island genetic algorithm (MIGA), to optimize the configuration of a universal selective solar absorber, which can avoid the premature phenomenon and superior to traditional genetic algorithm.

In the process of system design, the best system parameters shall be opted in an efficient and cost-effective way. Accordingly, besides the system design, the parametric analysis, optimization, and decision makings of the system must be implemented before any prototype construction begins. The literature overview divulges although some studies have been conducted on the solar-based energy systems theoretically and experimentally, no research has been done on the Energy–Exergy analyses, performance-based SOO and MOO processes, and MCDA of the IDX-SAHPs, altogether. Because these systems are new, studies on them are not enough, and thus, there is still a lot of potential for research on them. The main objectives of this research are:

- Developing the numerical modeling of the IDX-SAHP performance
- Carrying out the SA of the design parameters using OPAT
- Performing the energy–exergy analyses on the IDX-SAHP
- Performing the SOO and MOO approaches on the IDX-SAHP performance using NSGA-II
- Selecting the optimal layout of the IDX-SAHP using AHP MCDA coupled with the NSGA-II

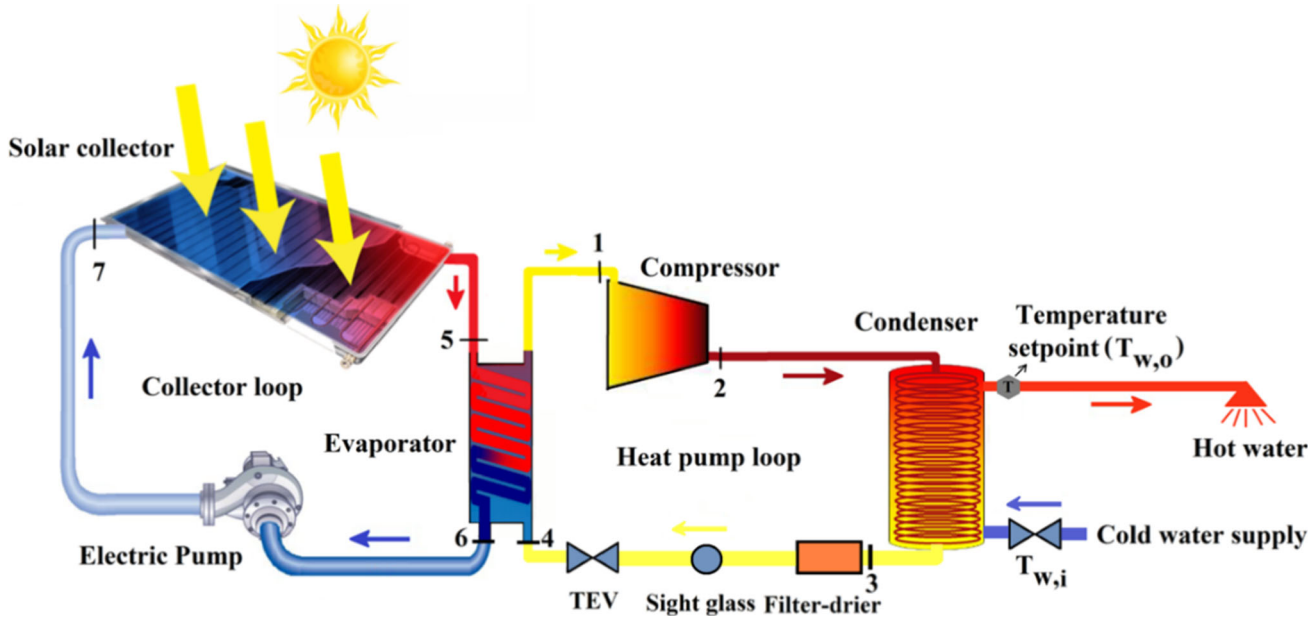

Fig. 1 The schematic view of the proposed IDX-SAHP system

- Comparing the performance of the maximized IDX-SAHP with the initial system

2 Materials and Methods

2.1 IDX-SAHP Description

Figure 1 depicts the schematic view of the proposed IDX-SAHP system. The IDX-SAHP under investigation has three separate loops. The collector loop includes the collector, pump, and an evaporator utilizing the 50 − 50% GWS by volume as the working substance. The evaporator is the joint equipment put between the solar collector and the heat pump loops. The heat pump loop includes a compressor, a condenser, a filter-drier, a thermostatic expansion valve (TEV).

During the IDX-SAHP operation, the GWS passes through the solar collector by the pump and obtains the ambient and solar energies (Fig. 1: from 7 to 5). The GWS passing through the evaporator shell delivers its energy to the R-134a refrigerant in the evaporator tubes (Fig. 1: from 5 to 6). Accordingly, the R-134a superheats after obtaining the GWS heat (Fig. 1: from 4 to1) and then enters the compressor to increase its pressure as much as the condenser pressure (Fig. 1: from 1 to 2). Thereupon, the superheated R-134a passes through the condenser tubes and is condensed by the water passing through the condenser shell (Fig. 1: from 2 to 3). The condensed R-134a then enters the TEV to decrease its pressure as much as the evaporator pressure (Fig. 1: from 3 to 4). Ultimately, the low-pressure and low-temperature R-134a re-enters the evaporator tubes and the IDX-SAHP cycle is ended. Table 1 provides the design parameters of the IDX-SAHP.

2.2 Assumptions

- Steady-state process.
- The process of passing the R-134a through the compressor is taken into account polytropic.
- The process of passing the R-134a through the TEV is taken into account isenthalpic.
- No pressure drops in the IDX-SAHP cycle.
- $T_{W,i} = T_a$.

2.3 Collector Modeling

The heat rate absorbed by the solar collector ($\dot{Q}_{cl}$) is determined as per the difference between the average temperatures of the collector plate (T_p) and the ambient air (T_a) as follows [32]:

$$\dot{Q}_{cl} = A_{cl} S - \dot{Q}_{\text{loss}} \tag{1}$$

$$\dot{Q}_{\text{loss}} = A_{cl} U_L \left(T_p - T_a\right) \tag{2}$$

Also, $\dot{Q}_{cl}$ can be defined as per the difference between the average temperatures of the GWS (T_{gw}) and the ambient air (T_a):

$$\dot{Q}_{cl} = A_{cl} F' S - A_{cl} F' U_L \left(T_{gw} - T_a\right) \tag{3}$$

Table 1 Design parameters of the IDX-SAHP

Parameter	Value
Solar intensity (I_T)	700 (W/m^2),Variable
Ambient temperature (T_a)	22°C, Variable
Inlet water temperature of the condenser ($T_{W,i}$)	22 ° C,Variable
Outlet water temperature of the condenser ($T_{W,o}$)	50° C,Variable
Specific heat capacity of the water (C_{pw})	4187 (J/kg.K)
Compressor speed (ω)	1750 (rpm), Variable
Compressor efficiency (η_{cm})	0.75
Collector area (A_{cl})	5.5(m^2), Variable
Wind speed (u_w)	3.1 (m/s)
Water volume in the condenser shell	270 (liter)
Mass flow rate of glycol − water solution ($\dot{m}_{gw}$)	77 (kg/hr)
Specific Heat of glycol − water solution ($C_{p,gw}$)	3.5\, (J/g·°C)
Power consumption of pump ($\dot{W}_{pump}$)	60 (Watt)
Polytropic index of $R-134a$ (k)	1.106
Absorptivity of collector plate (α)	0.9
Emittance of plate surface (ε_p)	0.1
Glass emittance factor (ε_g)	0.88
Thermal conductivity of collector plate (k_p)	250 (W/m.K)
Number of glass covers (N_{gl})	0, Variable
Displacement volume of compressor (V_d)	17.4 (cm3/rev)
Volumetric efficiency (η_v)	0.8
Diameter of the tube in collector plate (D_{cl})	9.4 (mm), Variable
Length of collector tube (L_{cl})	12 (m)
Length of copper tube in the condenser (L_{cond})	30 (m), Variable
Diameter of the copper tube in the condenser (D_{cond})	9.9 (mm)
Overall heat transfer coefficient of the evaporator (U_{eva})	$$12.6 (W/m^2·K)
Heat transfer surface area of the evaporator ($A_{s,eav}$)	2.77 (m^2)
Thickness of absorber of collector plate (δ)	0.004 (m), Variable
Collector tilt angel (β)	30 (deg)

where

$$S = I_T(\tau\alpha) \tag{4}$$

$$T_{gw} \approx \frac{T_5 + T_7}{2} \tag{5}$$

If $N_{gl} = 0$, then $\tau = 1$. Also, U_L is defined as:

$$U_L = \left(\frac{N_{gl}}{\frac{C}{T_{pm}}\left[\frac{(T_p - T_a)}{N_{gl}+f}\right]^e} + \frac{1}{h_w} \right)^{-1} + \frac{\sigma\left(T_p + T_a\right)\left(T_p^2 + T_a^2\right)}{\frac{1}{\varepsilon_p + 0.0059 N_{gl} h_w} + \frac{2N + f - 1 + 0.133\varepsilon_p}{\varepsilon_g} - N_{gl}} \tag{6}$$

here,

$$h_w = 5.7 + 3.8u_w \tag{7}$$

$$C = 520 \times \left(1 - 0.000051\beta^2\right) \tag{8}$$

$$e = 0.43 \times \left(1 - \frac{100}{T_{pm}}\right) \tag{9}$$

$$f = \left(1 + 0.089h_w - 0.1166h_w\varepsilon_p\right)\left(1 + 0.07866N_{gl}\right) \tag{10}$$

Additionally, the collector efficiency factor (F') is calculated as:

$$F' = \left[(1 - F)\frac{D_{cl}}{W}\right] + F \tag{11}$$

where

$$F = \frac{tanh(R(W - D_{cl})/2)}{R(W - D_{cl})/2} \tag{12}$$

$$R = \left(\frac{U_L}{K_p \delta}\right)^{0.05} \tag{13}$$

here, F is called the absorber fin efficiency and R is a fixed coefficient. Furthermore, the $\dot{Q}_{cl}$ can be calculated as follows:

$$\dot{Q}_{cl} = \dot{m}_{gw} C_{p,gw} (T_5 - T_7) \tag{14}$$

Considering $T_{gw} \approx \frac{T_5+T_7}{2}$ and the given mass flow rate of GWS ($\dot{m}_{gw}$) and specific heat of GWS ($C_{p,gw}$) in Table 2, T_5 and T_7 can be obtained.

2.4 Evaporator Modeling

The first law of thermodynamics for the solar collector loop may be presented as:

$$\dot{Q}_{\text{eva}} = \dot{Q}_{cl} + \dot{W}_{\text{pump}} \tag{15}$$

The heat transfer rate through the evaporator based on the glycol side was calculated from the $\dot{m}_{gw}$, $C_{p,gw}$, and the GWS temperature at each side of the evaporator as follows:

$$\dot{Q}_{\text{eva}} = \dot{m}_{gw} C_{p,gw} (T_5 - T_6) \tag{16}$$

Also, the heat rate transferred from GWS to the R-134a ($\dot{Q}_{eva}$) can be obtained by the energy balance across the evaporator as follows [30]:

The $\dot{Q}_{eva}$ can also be determined through Newton's law of cooling as [33]:

$$\dot{Q}_{\text{eva}} = U_{eva} A_{s,eav} \Delta T_m \tag{17}$$

$$\Delta T_m = \frac{(T_5 - T_4) - (T_6 - T_4)}{\ln\left(\frac{T_5 - T_4}{T_6 - T_4}\right)} \tag{18}$$

where U_{eva} is the overall heat transfer coefficient, $A_{s,eav}$ is the surface area of heat transfer, of the evaporator, and ΔT_m is the logarithmic average of the temperature difference between the GWS and R-134a streams at each end of the evaporator. It should be noted that the phase of R-134a changes from two-phase (point 4) to saturated vapor (point 1), at a constant temperature and constant pressure, namely, $T_4 = T_1$ and $P_4 = P_1$. In this regard, T_1 and P_1 (the temperature and pressure at the inlet of the compressor in saturated vapor state) may be obtained. Moreover, the $\dot{Q}_{eva}$ can be calculated as:

$$\dot{Q}_{eva} = \dot{m}_r (h_1 - h_4) \tag{19}$$

$$\dot{m}_r = \frac{\omega \eta_v V_d}{60 v_1} \tag{20}$$

2.5 Compressor Modeling

The compressor power ($\dot{W}_{cm}$) is determined as:

$$\dot{W}_{\text{cm}} = \dot{m}_r \frac{P_1 v_1}{\eta_{\text{cm}}} \frac{k}{k-1} \left(\left(\frac{P_2}{P_1} \right)^{\frac{k}{k-1}} - 1 \right) \tag{21}$$

where P_1 and P_2 are the pressures of R-134a at the inlet and outlet of the compressor.

2.6 Condenser Modeling

The heat rate delivered from R-134a in the condenser tubes to the water in the condenser shell ($\dot{Q}_{\text{cond}}$) can be obtained as follows:

$$\dot{Q}_{\text{cond}} = \dot{m}_r (h_2 - h_3) \tag{22}$$

In addition, $\dot{Q}_{\text{cond}}$ equals the heat rate absorbed by the water in the condenser shell from R-134a in the condenser tubes ($\dot{Q}_W$):

$$\dot{Q}_W = M_W C_{p,w} \frac{T_{W,o} - T_{W,i}}{\Delta t} = \dot{m}_r (h_2 - h_3) \tag{23}$$

here M_W and $C_{p,w}$ are, respectively, the water mass passing through the condenser shell and the specific heat capacity of the water. Moreover, $T_{W,i}$ and $T_{W,o}$ are the mean water temperature at the inlet and outlet of the condenser shell, respectively. As per the first law of thermodynamics in heat pump loop:

$$\dot{Q}_{\text{cond}} = \dot{Q}_W = \dot{Q}_{\text{eva}} + \dot{W}_{cm} \tag{24}$$

Additionally, Δt is the working hour of the IDX-SAHP to maintain the $T_{W,o}$ fixed:

$$\Delta t = \frac{\dot{m}_r (h_2 - h_3)}{M_W C_{p,w} (T_{W,o} - T_{W,i})} \tag{25}$$

Table 2 Equations of exergy analysis for each component of the proposed IDX-SAHP

System component	Input exergy (kW)	Output exergy (kW)	Exergy destruction (kW)	Exergy efficiency (η_{ex})	Equation No
Solar collector	$\dot{E\chi}_{rad}$	$\dot{m}_{gw}(\psi_{r5}-\psi_{r6})$	$\dot{E\chi}_{rad}-\dot{m}_{gw}(\psi_{r5}-\psi_{r6})$	$\frac{\dot{m}_{gw}(\psi_{r5}-\psi_{r6})}{\dot{E\chi}_{rad}}$	(31)
Compressor	$\dot{W}_{cm}$	$\dot{m}_r(\psi_{r2}-\psi_{r1})$	$\dot{W}_{cm}-\dot{m}_r(\psi_{r2}-\psi_{r1})$	$\frac{\dot{m}_r(\psi_{r2}-\psi_{r1})}{\dot{W}_{cm}}$	(32)
Condenser	$\dot{m}_r(\psi_{r2}-\psi_{r3})$	$\dot{Q}_{cond}(1-\frac{2T_0}{T_{W,o}+T_{W,i}})$	$\dot{m}_r(\psi_{r2}-\psi_{r3})-\dot{Q}_{cond}(1-\frac{2T_0}{T_{W,o}+T_{W,i}})$	$\frac{\dot{Q}_{cond}(1-\frac{2T_0}{T_{W,o}+T_{W,i}})}{\dot{m}_r(\psi_{r2}-\psi_{r3})}$	(33)
Evaporator	$\dot{m}_{gw}(\psi_{r5}-\psi_{r6})$	$\dot{m}_r(\psi_{r1}-\psi_{r4})$	$\dot{m}_{gw}(\psi_{r5}-\psi_{r6})-\dot{m}_r(\psi_{r1}-\psi_{r4})$	$\frac{\dot{m}_r(\psi_{r1}-\psi_{r4})}{\dot{m}_{gw}(\psi_{r5}-\psi_{r6})}$	(34)
TEV	$\dot{m}_r\psi_{r3}$	$\dot{m}_r\psi_{r4}$	$\dot{m}_r(\psi_{r3}-\psi_{r4})$	$\frac{\dot{m}_r\psi_{r4}}{\dot{m}_r\psi_{r3}}$	(35)

2.7 TEV Modeling

As TEV is isenthalpic, thus:

$$h_3 = h_4 \tag{26}$$

here h_3 and h_4 are, respectively, the enthalpies of R-134a at the input and output of the TEV.

2.8 COP and CE

The COP and CE of the system are determined as:

$$\mathrm{COP} = \frac{\dot{Q}_{\mathrm{cond}}}{\dot{W}_{\mathrm{cm}} + \dot{W}_{\mathrm{pump}}} \tag{27}$$

$$\mathrm{CE} = \frac{\dot{Q}_{cl}}{I_T A_{cl}} \tag{28}$$

2.9 Computational Flow Diagram

In the current research, the thermodynamic traits of the R-134a are utilized from the formulas presented by Cleland [34]. Additionally, energy equation solver (EES) software [35] is utilized to obtain the thermodynamic traits of the GWS. Figure 2 depicts the flow diagram to compute the COP and CE. As is evident in Fig. 2, first, an initial guess is made for T_{gw} to estimate the $\dot{Q}_{\mathrm{cl}}$ using Eqs. (1–14). In this regard, $\dot{Q}_{eva}$ is achieved using Eq. (15). Also,T_5 and T_7 can be obtained through Eqs. 3 and 14. Next, T_4 that is equal to T_1 is obtained using Eqs. (16–18). As the temperature at the inlet of the compressor (T_1) is in saturated vapor state, thus, the pressure and the enthalpy of the R-134a at the inlet of the compressor (P_1, h_1) can be extracted. Besides, h_4 is obtained by Eq. (19). Similarly, as $h_3 = h_4$ (Eq. (26)) and also state 3 is the saturated liquid state, thus, all of R-134a properties at state 3, especially P_3, can be extracted. Because $P_2 = P_3$, thus $\frac{P_2}{P_1}$ is obtained to calculate $\dot{W}_{\mathrm{cm}}$ by Eq. (21). Moreover, $\dot{Q}_{cond}$ may be determined by Eqs. (24), and thus, the $T_{w,i}$ can be obtained for a constant $T_{w,o}$ by Eqs. 22 and 23. For the reason that the obtained $T_{w,i}$ is equal to T_a, hence if $\left|\mathrm{obtained}T_{w,i} - T_a\right| \leq tol$, then the T_{gw} is admissible and the flowchart loop ends.

Consequently, the COP and CE of the system are defined. Otherwise if $\left|\mathrm{obtained}T_{w,i} - T_a\right| > tol$, the artificial neural network (ANN) is utilized to guess a new T_{gw}. ANNs are computing systems inspired by the biological neural networks that constitute animal brains [36, 37]. In an ANN, there are three basic layers comprising input layer, hidden layer, and output layer, each of which include neurons. The neurons number of the input (output) layer equals to the number of inputs (outputs), while the neurons number of the hidden layers varies during the training process to obtain the optimum accuracy. The input layer is the first ANN layer and consists of input neurons that receives input data in the form of text, numbers, audio files, image pixels, and so on. These neurons send data to the deeper layers, which in turn will send the final output data to the last output layer. The hidden layers are in the middle of the ANN model. These hidden layers perform various types of mathematical calculations on the input data and identify patterns in it. In the output layer, the result is obtained by accurate calculations of the middle layer. Neurons are connected between layers through weights. In each neuron, all inputs from the preceding layer are weighted by the weights and added together, along with a threshold. The weights are modified by learning. The relationship between the outputs (y) and inputs (x_i), known as transfer function, is defined as [38]:

$$y = f\left(\sum_{i=1}^{n} w_i x_i - b\right) \tag{29}$$

here w_i are the weights of connection from the i$^{\mathrm{th}}$ neuron in the previous layer to the neuron and b is a threshold. Then, the activation function was applied to inculcate nonlinearity

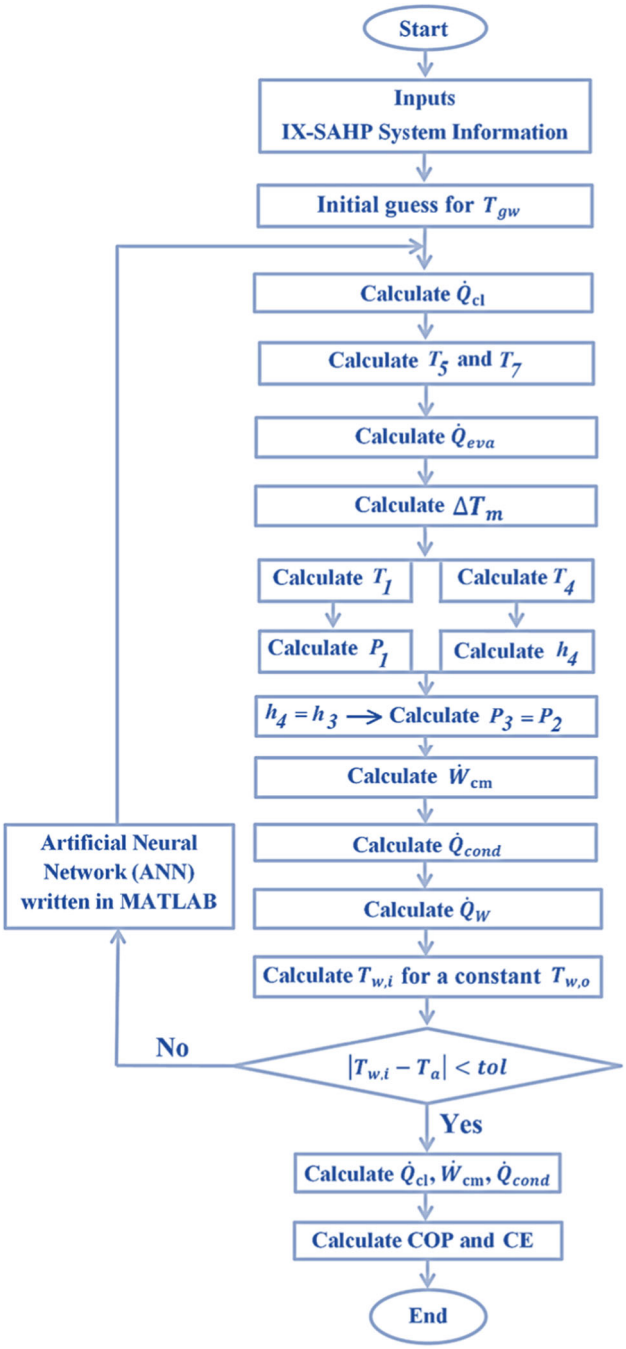

Fig. 2 Computational flow diagram to solve the proposed IDX-SAHP model

in the model and help the network learn any complex relationship between inputs and outputs. In this work, a tansig activation function was used as:

$$f(x) = \frac{1}{1 + \exp(-x)} \tag{30}$$

After getting the predictions from the output layer, the error is calculated, namely, the difference between the actual output (T_a) and the predicted output ($achievedT_{w,i}$). As ANN gathers its knowledge by detecting the patterns and relationships in data and learns through experience, thus, it can detect the T_{gw} as per its intelligent algorithm and the information obtained in previous iterations in such a way that $\left|achievedT_{w,i} - T_a\right| \leq tol$ (tolerance of 0.01). Accordingly, all of the thermodynamic traits of GWS and R-134a throughout the IDX-SAHP cycle are extracted, and therefore, CE and COP are defined.

Table 3 Ratio scale [56]

Value(A_{xy})	Description (x over y)
1	Equal importance
3	Weak importance
5	Strong importance
7	Very strong importance
9	Absolute importance
2, 4, 6, 8	Intermediate values

2.9.1 Thermodynamic Exergy Analysis

The exergy of a system ($\dot{E}\chi$) is the maximum useful work possible during a process that brings the system into equilibrium with a heat reservoir, reaching maximum entropy [39]. The real thermodynamic inefficiencies in an energy conversion system are related to exergy destruction and exergy loss. An exergy analysis determines the system components with the largest exergy destruction and the processes that cause them. The equations for input exergy, output exergy, exergy destruction (irreversibility) as well as the exergy efficiency of each component of the proposed IDX-SAHP are defined in Table 3 [33].

In the equations presented in Table 3, T_0 is the dead state temperature and is considered to be equal to the ambient temperature (T_a). Also, ψ_r is the specific stream exergy of the refrigerant and $\dot{E\chi}_{rad}$ is the exergy of solar radiation entering the solar collector defined as [40]:

$$\dot{E}\,\chi_{rad} = A_{cl} I_T \left[1 + \frac{1}{2}\left(\frac{T_0}{T_{sr}}\right)^4 - \frac{4}{3}\left(\frac{T_0}{T_{sr}}\right)\right] \tag{31}$$

Here, T_{sr} is the temperature of solar radiation which is 6,000 Kelvin.

The exergy efficiency of the system (η_{ex-sys}) is defined as the ratio of the exergy rate obtained from the heating of the water in the condenser to the sum of the electrical work of the compressor and pump plus the exergy of the solar radiation entering the collector, as follows [33]:

$$\eta_{ex-sys} = \frac{\dot{Q}_{cond}\left(1 - \frac{2T_0}{T_{W,o}+T_{W,i}}\right)}{\dot{W}_{cm} + \dot{W}_{pump} + \dot{E}\chi_{rad}} \tag{32}$$

The exergy destruction of the system ($\dot{E\chi}_{des-sys}$) is also defined as the sum of the irreversibilities of all system components as follows:

$$\dot{E}\chi_{\text{des - sys}} = \dot{E}\chi_{\text{des - cl}} + \dot{E}\chi_{\text{des - cond}} + \dot{E}\chi_{\text{des - eva}} + \dot{E}\chi_{\text{des - cm}} + \dot{E}\chi_{\text{des - TEV}} \tag{33}$$

2.9.2 Simulation-Based Optimization Approach

Figure 3 depicts the integration framework of the simulation-based optimization approach. As depicted, the thermodynamic model of the proposed system is derived and programmed using MATLAB programming language. The inputs of the MOO problem are the design parameters, decision parameters, and boundaries of decision parameters (constraints) [41, 42]. NSGA-II algorithm [43, 44, 45] was programed in MATLAB and coupled with the IDX-SAHP code to run the thermodynamic model and extract the outputs of the system, i.e., COP and CE (fitness functions). Afterward, NSGA-II gathers the simulation results [$F(X_i)$] and their relevant decision variables (X_i), and then sorts them as per its computational intelligence algorithm to identify the better X_i through an efficient heuristic search [46, 47, 48]. Next, MATLAB enters the new achieved X_i into the IDX-SAHP model and makes it run to extract the new $F(X_i)$. This process runs on till the termination criteria are reached, namely, the maximum number of iterations of 100 is met or the average rate of change in the spread of the Pareto curve becomes less than the tolerance of 0.001. These termination criteria are chosen as per several pre-tests to attain the best trade-off between the running time and the accuracy of the Pareto curve [43, 49, 50].

The NSGA-II coupled to the IDX-SAHP model leads to achieving the Pareto curve which represents the optimal non-dominated solutions [49, 51]. Finally, the best solution among all optimal solutions on the Pareto curve is chosen by the analytic hierarchy process (AHP) MCDA [52, 53] programmed under the MATLAB environment [54]. The principle of the AHP method is to make pairwise comparisons of the diverse alternatives and criteria to achieve their relative weights and to make the best decision among the alternatives [55]. The steps of AHP implementation are as follows [56]:

Step 1: The decision-making problem is organized as a hierarchy and is divided into three main levels including:

- First level: the objective of the decision-making problem lies at the first of the hierarchy structure. In this work, the objective is the selection of a single optimum solution for the final configuration.
- Second level: the criteria lie at the second level of the hierarchy, which are the fitness functions including COP (F_1) and CE (F_2)
- Third level: the alternatives lie at the third level of the hierarchy structure, which are the Pareto-optimal solutions.

Step 2: The fitness functions are compared to the pairwise to evaluate their weights through the ratio scales listed in Table 4. The pairwise comparison matrix A is organized as per the decision maker's judgments (A_{xy}), as follows:

$$A = \begin{bmatrix} 1 & A_{12} & \dots & A_{1n} \\ A_{21} & 1 & \dots & A_{2n} \\ \dots & \dots & 1 & \dots \\ A_{n1} & \dots & \dots & 1 \end{bmatrix} \text{where}$$

$$A_{xy} = 1/A_{yx};\ x,\ y = 1,\ 2,\ 3,\ \dots,\ n \tag{34}$$

Step 3: Define the maximum eigenvalue ($\lambda_{\max}$) of the judgment matrix (A_{xy}) as follows:

$$\det(A - \lambda A) = 0 \tag{35}$$

Step 4: Compute the consistency index (CI) as follows:

$$CI = \frac{\lambda_{\max} - n}{1 - n} \tag{36}$$

Here, and n is the order of the A_{xy} matrix.

Step 5: Calculate the consistency ratio (CR) to check judgment consistencies. Judgments are acceptable for CR values less than 0.1.

$$CR = \frac{CI}{RI} \tag{37}$$

RI is the average random consistence indicator of the A_{xy} matrix.

Step 6: Calculate the weight vector, as follows:

$$M_i = \prod_{x=1}^{n} A_{xy}\ x = 1,\ 2,\ 3,\ \dots,\ n \tag{38}$$

$$\overline{w_N} = \sqrt[n]{M_x}\ x = 1,\ 2,\ 3,\ \dots,\ n \tag{39}$$

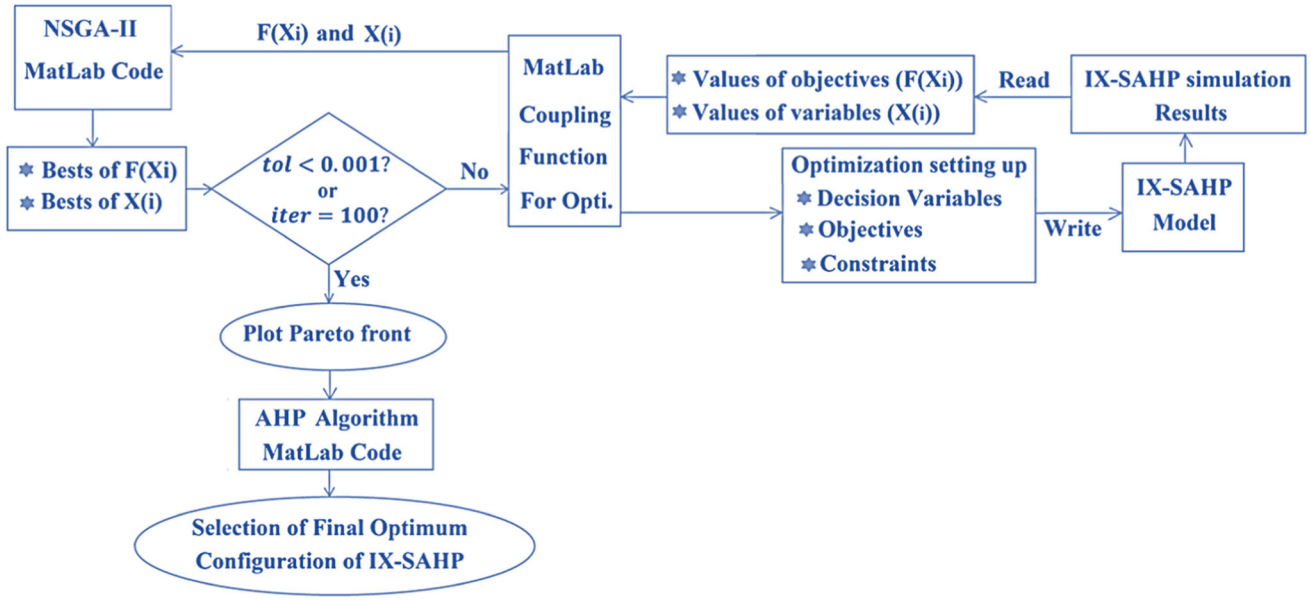

Fig. 3 Integration framework of simulation-based optimization approach

Table 4 Decision parameters and their boundaries

Variable	Unit	Baseline value	Rage of variations
A_{cl}	m^2	5.5	[1.5, 6.5]
ω	(rpm)	1750	[1200, 2800]
L_{cond}	m	30	[20, 60]
D_{cl}	(mm)	9.4	[9, 21]
δ	(mm)	4	[1, 10]
k_p	(W/m.K)	250	[200, 400]

Step 7: Normalized weight vector ($\overline{w_N}$), as follows:

$$W_x = \frac{\overline{w_N}}{\sum_{x=1}^{n} \overline{w_N}} \tag{40}$$

W_i is the relative weight coefficient of each factor.

$$\mathrm{W} = [\mathrm{w}_1,\ \mathrm{w}_2,\ \ldots,\ \mathrm{w}_n]^{\mathrm{T}} \tag{41}$$

Step 8: Evaluate the solutions on the Pareto curve as per the W_x of each criterion, and then obtain a single optimum solution for the final configuration.

It should be noted because of the variations range of the decision variables, the number of feasible configurations of the IDX-SAHP is countless, while the proposed simulation-based multiple-criteria optimization method leads to lessening the running time substantially compared to numerous searches.

2.9.3 Fitness Functions and Decision Parameters

In the current research, CE and COP are chosen as two fitness functions with equally important weight. Additionally, the decision parameters and their boundaries are presented in Table 5. It should be noted that the decision parameters and their boundaries were opted as per several grounds comprising the working experiences of the authors in heating, ventilation, and air conditioning (HVAC) laboratories and companies, scrutinizing a good deal of simulations and experimental investigations [27, 28, 32, 71] and published books [57–60] concerning SAHPs, the available equipment in the market, and design restrictions.

3 Climate Characteristics of the Studied City

Tehran is the capital of Iran with a population of around 8.7 million in the city and 15 million in the larger metropolitan area of Greater Tehran and is the most populous city and the most energy consuming city in Iran [61, 62]. In the current investigation, Tehran with a temperate climate characteristic is opted to analyze and optimize the IDX-SAHP performance. The climate characteristics of Tehran are presented in Table 6.

Table 5 Climate characteristics of Tehran, Iran [66]

Month	T_a	I_T	u_w	Monthly Sunshine Hours (MSHs)
January	6	317.1276	2.8	170
February	6	391.942	2.9	189
March	10	411.2012	2.9	207
April	17	456.0156	2.8	223
May	22	490.7376	3.1	270
June	28	550.81	3	300
July	31	570.552	3.1	343
August	30	562.4964	3.2	330
September	26	524.7188	3.5	320
October	19	467.5896	3.6	218
November	11	379.6272	2.7	178
December	5	307.8684	2.8	161

Table 6 Results achieved by the SOOs and MOO

Opt. method	Variables						Objectives		Performance index
	$A_{cl}m^2$)	ω(rpm)	L_{cond}(m)	D_{cl}(mm)	k_p(W/m.K)	δ(mm)	CE(%)	COP	Operating hours(hour)
Baseline model	5.5	1750	30	9.4	250	4	52	3	1319
CE based on single max.	1.51	2780	45	11.5	399	9.5	91	1.5	1258
COP based on single max.	6.5	1205	50	12.95	395	9.0	42	8.7	1101
NSGA-II coupled to AHP	6.35	1430	48	12.95	390	8.7	46.4	7	1037

4 Results and Discussion

This section compromises five parts. In the first part, the performance evaluation of the developed IDX-SAHP performance is performed. In the second part, the SA of the design parameters (pre-optimization) [63–65] comprising T_a, I_T, $T_{W,o}$, ω, A_{cl}, k_p, N_{gl}, D_{cl}, L_{cond}, and δ is carried out using OPAT technique. Then in the third part, the exergy analysis of the IDX-SAHP is investigated. In addition, in the fourth part, the SOO and MOO on the IDX-SAHP performance are implemented using NSGA-II. Afterward, the best configuration for the IDX-SAHP is opted using AHP MCDA. Finally, in the fifth part of the work, performance of the maximized IDX-SAHP is compared to the initial one.

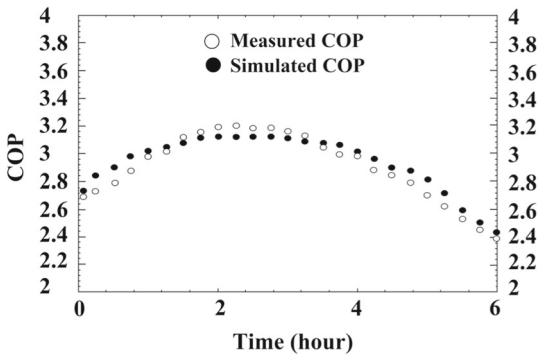

Fig. 4 COP obtained by the numerical modeling and the experiment

4.1 Verification

To verify the IDX-SAHP, the parameters of the developed IDX-SAHP are opted as the specifications of IDX-SAHP system built by Bridgeman [27]. Then, the COP, $\dot{W}_{m}athrmcm$, $\dot{Q}_{m}athrmcond$, and $\dot{Q}_{m}athrmeva$ of the developed IDX-SAHP were compared to the Bridgeman experimental work [27]. Figures 4 and 5 indicate the values achieved by the numerical model and the experimental values achieved by Bridgeman [27]. As shown, the experimental values of the COP, $\dot{W}_{\text{cm}}$, $\dot{Q}_{\text{cond}}$, and $\dot{Q}_{\text{eva}}$ are almost the values achieved by the numerical model with the relative errors of 6%, 12%, 15%, and 11%, respectively. The reason for the small difference between numerical modeling and experimental values

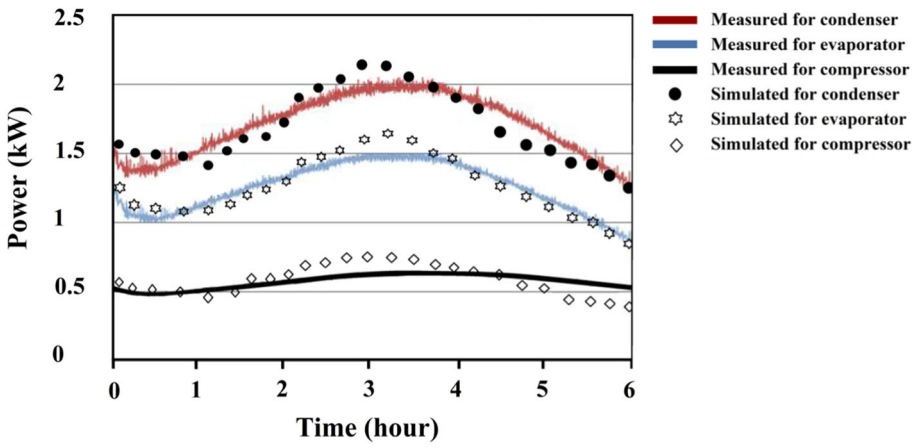

Fig. 5 $\dot{W}_{cm}$, $\dot{Q}_{cond}$, and $\dot{Q}_{eva}$ obtained by the numerical modeling and the experiment

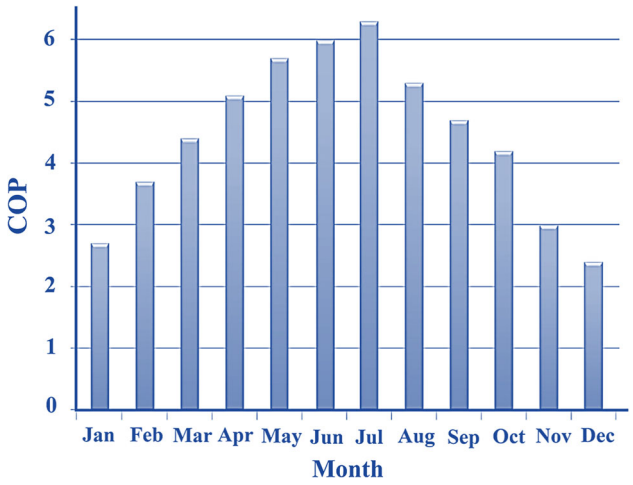

Fig. 6 COP per month

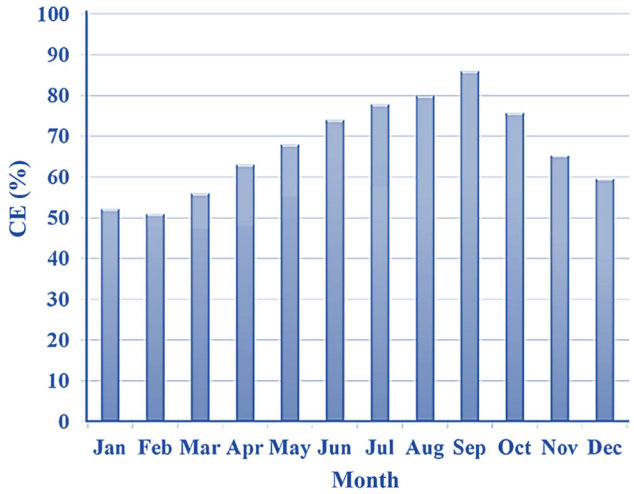

Fig. 7 CE per month

may be due to the losses in the IDX-SAHP elements, in particular in the piping system.

4.2 Performance Evaluation

To evaluate the monthly performance of the developed IDX-SAHP, $T_{W,i}$ and T_a were taken into account the same, and $T_{W,o}$ was kept constant at 50° C. Other IDX-SAHP characteristics are presented in Tables 1 and 4. Figures 6 and 7 present the COP and CE values per month. The highest COP is 6.3 in July with the highest values for T_a (31 $°C$), I_T (570.552 W/m^2), and MSHs (343 hours) throughout the year. Additionally, the smallest COP is 2.4 in December with the least values for I_T (307.8684 W/m^2), MSHs (161 hours), and T_a (5 $°C$) throughout the year. On the contrary, the largest CE is 86% in September with a small value for of I_T (524.7188 W/m^2), and almost high values for T_a (26 $°C$) and MSHs (320 hours) throughout the year. Furthermore, the least CE is 51% in February with a high value for I_T (391.942 W/m^2), and almost small values for T_a (6 $°C$) and MSHs (189 hours) throughout the year.

Also, Figs. 8 and 9 present, respectively, the working hour of the IX-SHHP and $\dot{Q}_{\text{cond}}$ per month. To have $T_{W,o}$ of 5 0 ° C, the total working hour is 1319 hours throughout the year and ranges from 74 hours in July to 143 hours in December. In addition, $\dot{Q}_{cond}$ ranges from 122kWh in July to 342kWh in December. In the warm months, the working hour and $\dot{Q}_{\text{cond}}$ is smaller because $T_{W,i}$, T_a, I_T, and MSHs are larger and vice versa.

4.3 Sensitivity Analysis (SA)

This part of the research gives the SA of main IDX-SAHP parameters such as T_a, I_T, $T_{W,o}$, ω, A_{cl}, k_p, N_{gl}, D_{cl}, L_{cond}, and δ using the OPAT technique [67, 68]. According to the OPAT, each time, one parameter changes over its boundaries and the other parameters are fixed at their initial values [69, 70] (as provided in Table 1) and the IDX-SAHP performance is assessed.

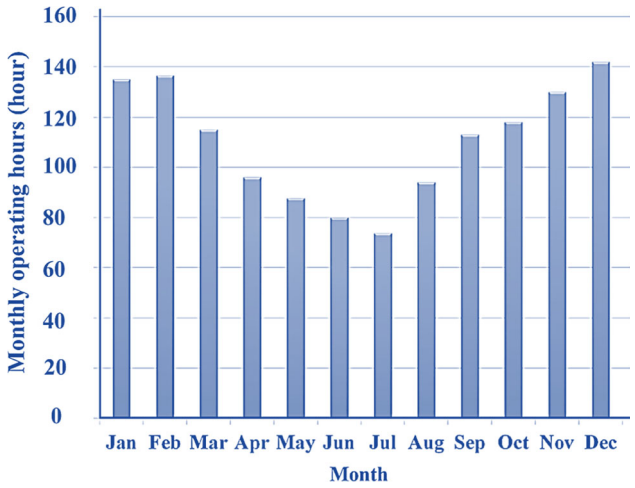

Fig. 8 Working hour per month

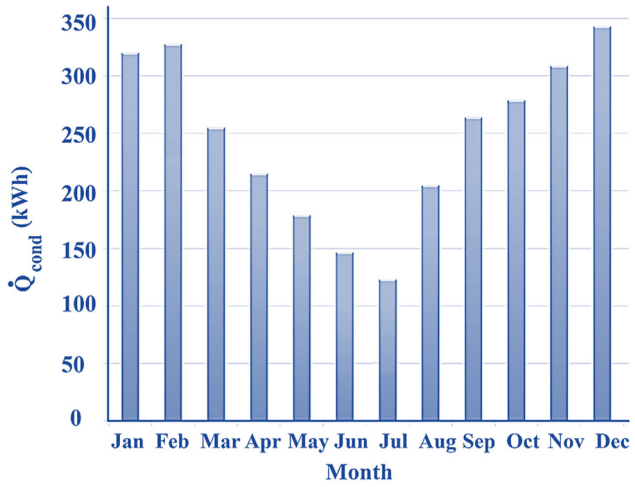

Fig. 9 $\dot{Q}_{\text{cond}}$ per month

4.3.1 Influence of T_a

Figure 10 depicts the influence of T_a on the IDX-SAHP performance. Increasing T_a at constant I_T enhances T_p and T_{gw}. Therefore, $\dot{Q}_{\text{loss}}$ decreases which leads to increase in CE. Additionally, by reducing $\dot{Q}_{\text{loss}}$, more heat rate is delivered to the GWS, and accordingly, to the R-134a passing through the evaporator tubes. In this regard, $\dot{W}_{\text{cm}}$ decreases which leads to increase in COP [32]. The COP-CE diagram of the developed IDX-SAHP in terms of T_a variations is in accordance with the results of the investigation conducted by Kong et al. [32].

4.3.2 Influence of I_T

Figure 11 depicts the influence of I_T on the IDX-SAHP performance. With the increase in I_T at constant T_a, the T_p is

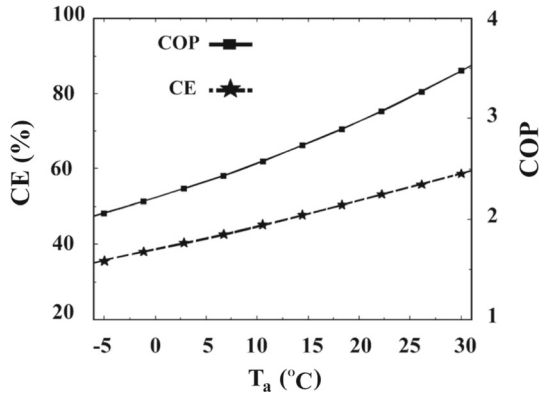

Fig. 10 Influence of T_a on the IDX-SAHP performance

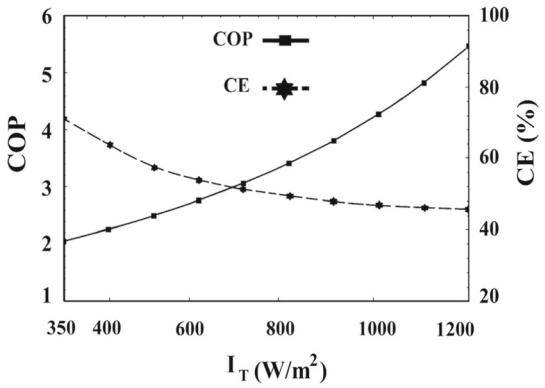

Fig. 11 Influence of I_T on the IDX-SAHP performance

enhanced. The higher T_p leads to increase $|T_p - T_a|$, and accordingly, $\dot{Q}_{\text{loss}}$ increases and thus CE reduces. Moreover, by increasing the I_T, the $\dot{Q}_{cl}$ is enhanced. Consequently, T_{gw} increases and the GWS obtains more energy from the solar collector, and accordingly, the heat is delivered more to the R-134a passing through the evaporator tubes. Consequently, $\dot{W}_{\text{cm}}$ reduces which leads to increase in COP [32, 71]. The COP-CE diagram of the developed IDX-SAHP in terms of I_T variations is in accordance with the results of the investigation conducted by Kong et al. [32].

4.3.3 Influence of N_{gl}

Figure 12 depicts the influence of N_{gl} on the IDX-SAHP performance. With the increase in N_{gl} at constant T_a and I_T, the COP and CE enhance a little. The glass cover of the solar collector plays as a thermal insulation which traps the solar radiation and decreases $\dot{Q}_{\text{loss}}$, and accordingly, CE increases [72]. Furthermore, with the reduction of $\dot{Q}_{\text{loss}}$, the T_p is enhanced, and the GWS obtains more energy from the solar collector, and accordingly, the heat is delivered more to the R-134a passing through the evaporator tubes. Consequently, $\dot{W}_{\text{cm}}$ reduces which leads to increase in COP.

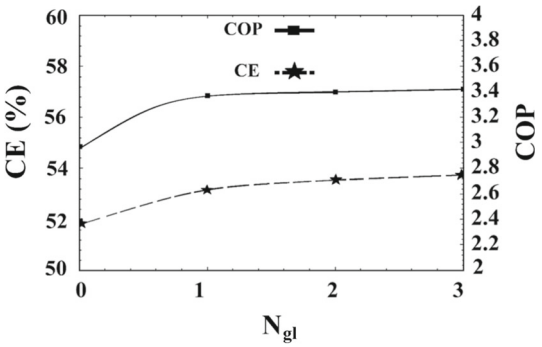

Fig. 12 Influence of N_{gl} on the IDX-SAHP performance

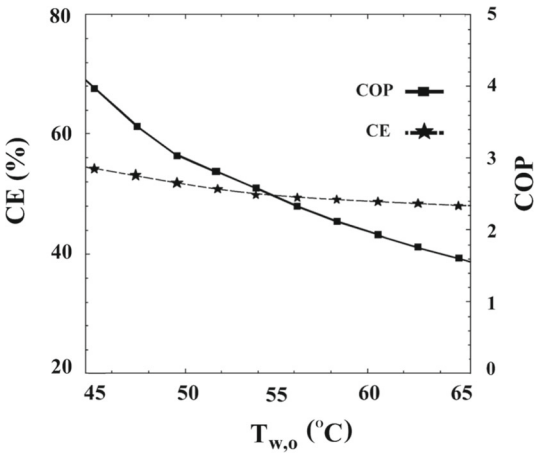

Fig. 13 Influence of $T_{W,o}$ on the IDX-SAHP performance

4.3.4 Influence of $T_{W,o}$

Figure 13 depicts the influence of $T_{W,o}$ on the IDX-SAHP performance. With the increase in $T_{W,o}$ at constant T_a and I_T, the $\dot{W}_{cm}$ is enhanced, and accordingly, COP lessens. Besides, the larger the $\dot{W}_{cm}$ the higher refrigerant enthalpy at the evaporator inlet. In this regard, the refrigerant capacity lessens in obtaining the energy from the GWS in the evaporator shell. Consequently, the GWS comes back to the solar collector at a larger temperature which leads to reducing in CE [32, 73].

4.3.5 Influence of A_{cl}

Figure 14 depicts the influence of A_{cl} on the IDX-SAHP performance. Increasing A_{cl} at constant T_a and I_T enhances $\dot{Q}_{cl}$ which leads to increase in T_{gw}. Accordingly, the GWS obtains more energy from the solar collector, and accordingly, the heat is delivered more to the R-134a passing through the evaporator tubes. Consequently, $\dot{W}_{cm}$ reduces which leads to increase in COP [32, 71]. Besides, the higher A_{cl} the higher $\dot{Q}_{loss}$, which leads to reduction of CE. The COP-CE diagram of the developed IDX-SAHP in terms of A_{cl} variations is in

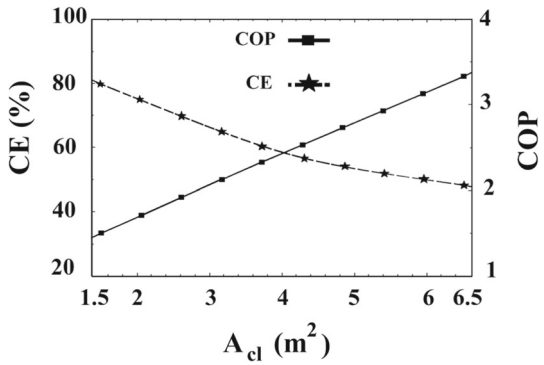

Fig. 14 Influence of A_{cl} on the IDX-SAHP performance

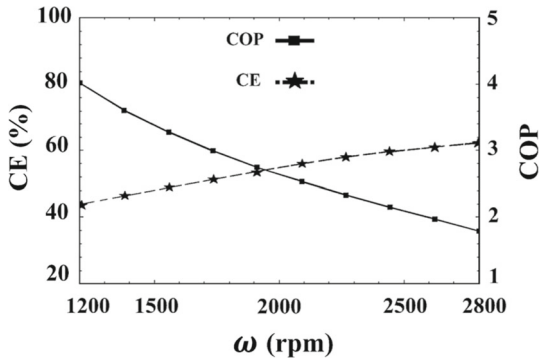

Fig. 15 Influence of ω on the IDX-SAHP performance

accordance with the results of the investigation conducted by Kong et al. [32].

4.3.6 Influence of ω

Figure 15 depicts the influence of ω on the IDX-SAHP performance. By increasing the ω at constant T_a and I_T, the temperature of R-134a at the compressor outlet and $\dot{W}_{cm}$ enhance which leads to reduction in COP. Additionally, the larger ω the larger R-134a mass flow rate ($\dot{m}_r$), and accordingly, the R-134a obtains more energy from the GWS passing through the evaporator tubes. In this regard, the GWS comes back to the solar collector at a lower temperature which leads to reduction in $\dot{Q}_{loss}$, and consequently the CE is enhanced. It is worth noting that decrease in COP and increase in CE by increasing ω indicate that there is an optimum ω to achieve an IDX-SAHP with the highest performance. The COP-CE diagram of the developed IDX-SAHP in terms of ω variations is in accordance with the results of the investigation conducted by Kong et al. [32].

4.3.7 Influence of the L_{cond}

Figure 16 depicts the influence of L_{cond} on the IDX-SAHP performance. Increasing L_{cond} at constant T_a and I_T leads

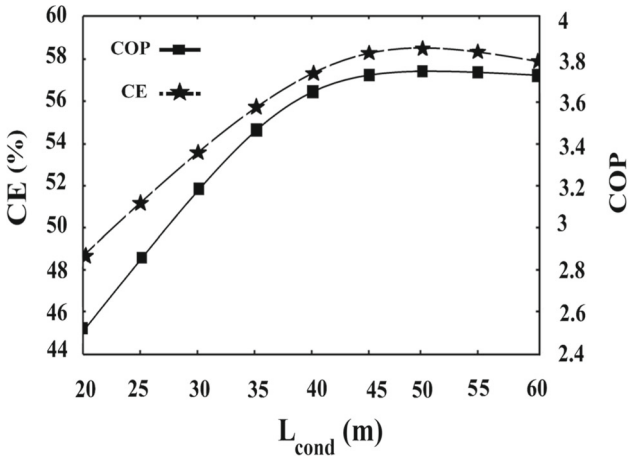

Fig. 16 Influence of L_{cond} on the IDX-SAHP performance

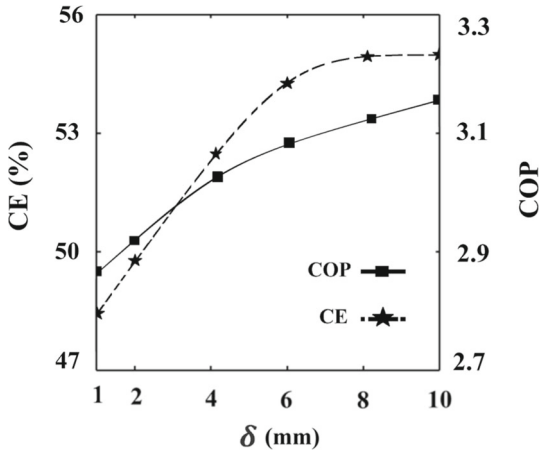

Fig. 18 Influence of δ on the IDX-SAHP performance

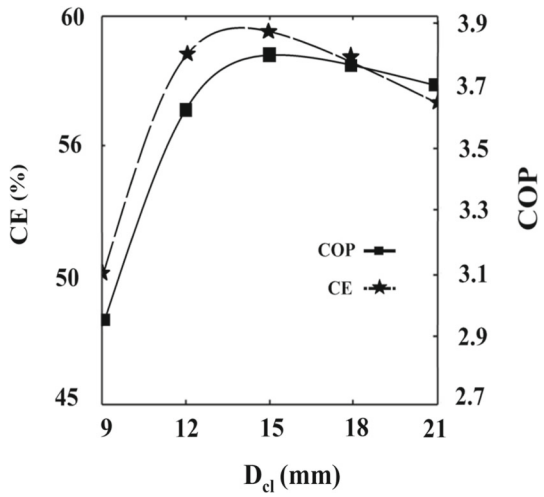

Fig. 17 Influence of D_{cl} on the IDX-SAHP performance

to increase in A_{coil}. In this regard, $\dot{Q}_{\text{cond}}$ is enhanced, and accordingly, $\dot{W}_{\text{cm}}$ lessens which leads to increase in COP. Further, the lower $\dot{W}_{\text{cm}}$ the lower R-134a enthalpy at the evaporator inlet. As a result, the refrigerant capacity is enhanced in obtaining the energy from the GWS in the evaporator shell. Consequently, the GWS comes back to the solar collector at a lower temperature which leads to increase in CE [32, 73]. Moreover, as depicted, the IDX-SAHP has the best performance in L_{cond} of 50(m). If $L_{\text{cond}} > 50(m)$, COP and CE would lessen since L_{cond} is larger enough, even redundantly, to deliver the thermal energy from the R-134a to the water. The COP-CE diagram of the developed IDX-SAHP in terms of L_{cond} variations is in accordance with the results of the investigation conducted by Zhang et al. [74].

4.3.8 Influence of D_{cl}

Figure 17 depicts the influence of D_{cl} on the IDX-SAHP performance. Increasing D_{cl} at constant T_a and I_T leads to increase the side surface of the collector tubes, and accordingly, the GWS gains more energy from the collector, resulting in increase of $\dot{Q}_{\text{cl}}$. In this regard, T_{gw} is enhanced, and therefore, the thermal energy is delivered more to the R-134a passing through the evaporator tubes. Consequently, $\dot{W}_{\text{cm}}$ lessens, and thus COP increases. Besides, the higher T_{gw} the lower $\dot{Q}_{\text{loss}}$ that leads to increase in CE. Also, as indicated, the IDX-SAHP has the best performance in D_{cl} of 13(mm). Because $D_{cl} > 13$(mm) is too big for the IDX-SAHP, resulting in $\dot{Q}_{\text{loss}}$ increase and GWS charge decrease, and consequently the COP and CE would lessen [74]. The COP-CE diagram of the developed IDX-SAHP in terms of D_{cl} variations is in accordance with the results of the investigation conducted by Zhang et al. [74].

4.3.9 Influence of δ and k_p

Figures 18 and 19, respectively, depict the influences of δ and k_p on the IDX-SAHP performance. By increasing the k_p and δ at constant T_a and I_T, the T_{gw} is enhanced due to the higher $\dot{Q}_{cl}$. Thus, the GWS obtains more energy from the collector, and accordingly, the heat is delivered more to the R-134a passing through the evaporator tubes. Consequently, $\dot{W}_{cm}$ reduces which leads to increase in COP [32, 71]. Besides, the higher T_{gw} the lower $\dot{Q}_{\text{loss}}$ which leads to increase in CE [72, 74]. Also, the higher k_p the lower temperature gradient in the collector plate. In this regard, by increasing the δ slightly, the accumulation of thermal energy in the collector plate would enhance a little, and consequently, COP and CE would enhance a little. The COP-CE diagram of the developed IDX-SAHP in terms of δ variations is in accordance with the results of the investigation conducted by Zhang et al. [74].

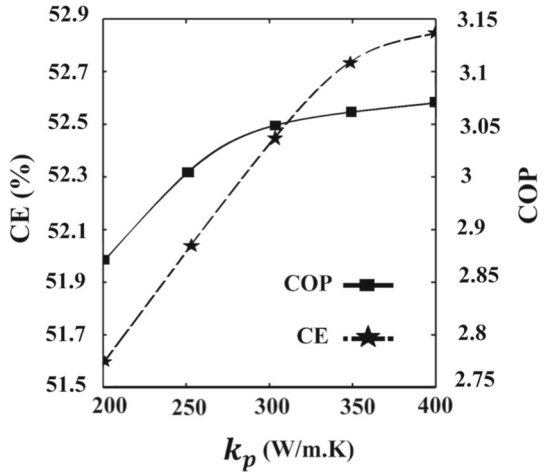

Fig. 19 Influence of k_p on the IDX-SAHP performance

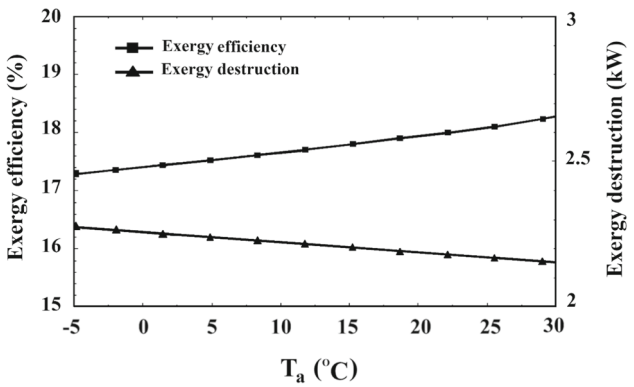

Fig. 20 Influence of T_a on the exergy efficiency and exergy destruction of the IDX-SAHP

The SA indicated that the performance of the IDX-SAHP would be noticeably affected by the design parameters. Consequently, the performance may be largely enhanced by selecting the appropriate IDX-SAHP parameters. In this regard, the parametric analysis reveals the behaviors of the system performance with the diverse input parameters and helps the designers and engineers to select the most appropriate materials for the system. However, to achieve the optimum IDX-SAHP, the MOO coupled to the MCDAs necessitates.

4.4 Exergy Analysis Results

In this section, the influence of various factors such as T_a, I_T, A_{cl} and ω on exergy efficiency (η_{ex-sys}) and exergy destruction ($\dot{E\chi}_{des-sys}$) of the IDX-SAHP system is investigated using the OPAT technique.

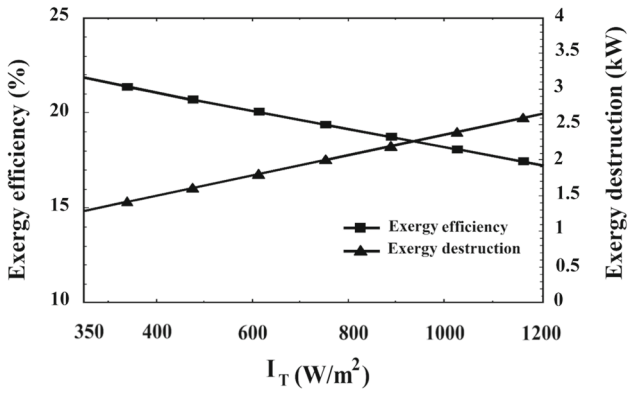

Fig. 21 Influence of I_T on the exergy efficiency and exergy destruction of the IDX-SAHP

4.4.1 Influence of T_a on η_{ex-sys} and $\dot{E\chi}_{des-sys}$

Figure 20 depicts the influence of T_a on exergy efficiency and exergy destruction of the system. Since $T_a = T_{w,i}$, thus, by increasing the T_a in constant I_T, the $T_{w,i}$ increases. Therefore, as $T_{w,o}$ is constant at 50° C, the difference between $T_{w,i}$ and $T_{w,o}$ is reduced and the amount of heat loss from the condenser is reduced, accordingly. In this regard, the exergy efficiency increases and the exergy destruction reduces. As observed, T_a had a very small influence on the system. On the other hand, by increasing T_a, the temperature difference between the collector surface and the environment decreases and heat loss from the collector surface decreases; this is beneficial in increasing exergy efficiency. As seen in Fig. 20, by increasing T_a from −5 to 30 °C in constant I_T, the system's exergy efficiency increases from 17.3 to 18.2% and the system's exergy destruction decreases from 2.25 to 2.15 kW.

4.4.2 Influence of I_T on η_{ex-sys} and $\dot{E\chi}_{des-sys}$

Figure 21 depicts the influence of I_T on exergy efficiency and exergy destruction of the system. With the increase in I_T at constant T_a, the T_p is enhanced. The higher T_p leads to increase $|T_p - T_a|$, and accordingly, $\dot{Q}_{loss}$ increases, and thus, CE reduces. Subsequently, the exergy destruction increases and the exergy efficiency reduces by increasing the $\dot{Q}_{\text{loss}}$. Moreover, as observed from Fig. 21, the influence of I_T on exergy efficiency and exergy destruction of the system is far greater than the influence of T_a. By increasing I_T from 350 W/m^2 to 1200 W/m^2 in constant T_a, the system's exergy efficiency decreases from 22% to 16.2% and the system's exergy destruction increases s from 1.25 kW to 2.5 kW.

4.4.3 Influence of A_{cl} on η_{ex-sys} and $\dot{E\chi}_{des-sys}$

Figure 22 depicts the influence of A_{cl} on exergy efficiency and exergy destruction of the system. With the increase in

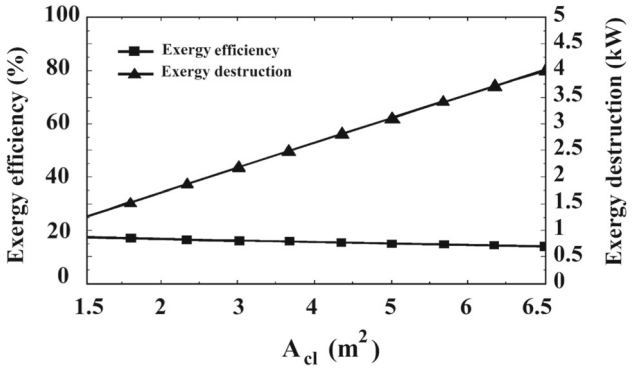

Fig. 22 Influence of A_{cl} on the exergy efficiency and exergy destruction of the IDX-SAHP

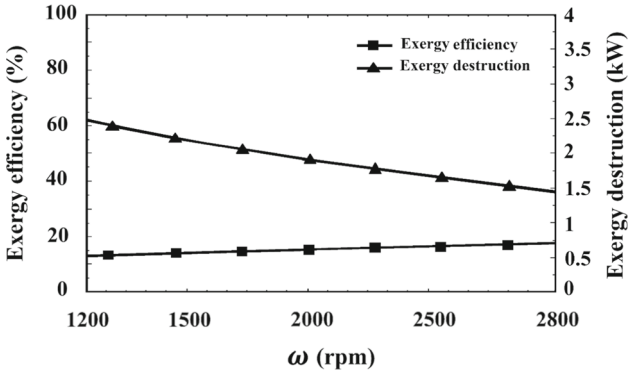

Fig. 23 Influence of ω on the exergy efficiency and exergy destruction of the IDX-SAHP

A_{cl} in constant T_a, the amount of $\dot{E\chi}_{rad}$ is enhanced as per. Accordingly, the exergy efficiency decreases and the exergy destruction increases. By increasing A_{cl} from 1.5 m^2 to 6.5 m^2 in constant T_a, the system's exergy efficiency decreases from 18 to 14% and the system's exergy destruction increases from 1.4 kW to 4 kW.

4.4.4 Influence of ω on η_{ex-sys} and $\dot{E\chi}_{des-sys}$

Figure 23 depicts the influence of ω on exergy efficiency and exergy destruction of the system. By increasing the ω in constant T_a and I_T, the temperature of R-134a at the compressor outlet enhances which leads to increase in $\dot{Q}_{\text{cond}}$. Therefore, the exergy efficiency increases and the exergy destruction in the condenser decreases. It should also be noted that as the ω increases, the compressor does more work and as a result, the rate of exergy destruction in the compressor increases; however, increasing the ω reduces the exergy destruction in the condenser. Considering the sum of all the irreversibilities of the system components, increasing the ω lead to decrease in the exergy destruction of the whole system. Accordingly, the influence of ω on the exergy destruction of condenser is larger than compressor. By increasing ω from 1200(rpm) m^2 to 2800(rpm) in constant T_a and I_T, the system's exergy efficiency increases from 14 to 18% and the system's exergy destruction decreases from 2.4 kW to 1.5 kW.

4.5 Optimization Results

This part of the research presents the results of the maximized IDX-SAHP. It should be noted that December month is opted to optimize the IDX-SAHP because of having the least amounts of I_T (307.8684 W/m^2), MSHs (161h), and T_a (5 °C) along with the highest amount of working hour (142h) throughout the year. Besides, the maximized IDX-SAHP is fully compared to the initial model.

4.5.1 SOO and MOO Results

Table 6 presents the SOOs and MOO results of the IDX-SAHP. In the COP-based maximization, the highest amount of A_{cl} (6.5 m^2) and the least amount of ω (1205 rpm) were achieved. However, CE-based maximization, the least amount of A_{cl}(1.5m^2) and the highest amount of ω (2780rpm) were achieved. Additionally, the L_{cond} of 50(m), D_{cl} almost 13.0(mm), k_p almost 400(W/m.K), and the δ of about 1.0(mm) were achieved through the SOOs for COP and CE.

The optimum parameters achieved by the COP-based maximization (provided in Table 6) were implemented in the initial IDX-SAHP model. The total working hour was 1101h throughout the year, resulting in 218hours reduction compared to the initial IDX-SAHP. Besides, the optimum parameters achieved by the CE-based maximization (provided in Table 6) were implemented to the initial IDX-SAHP model. The total working hour was 1258h throughout the year, resulting in 61h reduction compared to the initial IDX-SAHP. Accordingly, the design of IDX-SAHP based on the SOO of COP gave a better performance compared to the SOO of CE.

Similar to the achieved conclusion from the SA, the SOOs also showed there is an optimum A_{cl} and ω to achieve the highest performance for IDX-SAHP.

To scrutinize the COP and CE interactions, the MOO may be performed using the NSGA-II algorithm. Figure 24 presents the Pareto curve obtained by the MOO process which depicts the COP and CE interactions. As observed, as COP lessens, CE is enhanced and vice versa, namely, it is unfeasible to enhance both COP and CE, simultaneously.

As presented, the least COP is at point B with a value of 1.5 while CE has the largest amount with a value of 91%. Besides, the least CE is at point A with a value of 42% whereas COP has the largest amount with a value of 8.7. Accordingly, the optimum solutions obtained by the MOO process lay in $1.5 \leq COP \leq 8.7$ and $\%42 \leq CE \leq \%91$.

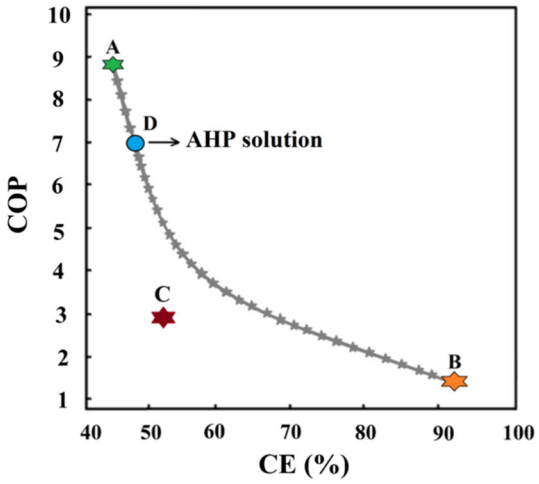

Fig. 24 Pareto curve obtained by the MOO process

To achieve the final optimum layout of the IDX-SAHP, the AHP MCDA method was integrated with the MOO process. Accordingly, an maximized IDX-SAHP with A_{cl} of $6.35m^2$, ω of 1430(rpm), L_{cond} of 48(m), D_{cl} almost 13.0(mm), k_p of 390(W/mK), and δ of about 8.7(mm) were yielded. In Fig. 24, point D and point C, respectively, represent the values of COP and CE of the maximized IDX-SAHP system and the initial one.

As presented in Table 6, in the SOO of COP, the COP is enhanced greatly from 3 to 8.7 whereas the CE lessened a little from 52% to 42%. Besides, in the SOO of CE, the COP lessened slightly from 3 to 1.5 whereas the CE is greatly enhanced from 52 to 91%. It is deduced that increasing the COP reduces the CE, and accordingly, both fitness functions cannot be improved at the same time. Furthermore, the AHP MCDA method integrated with the MOO process yielded that COP is largely enhanced from 3 to 7 whereas the CE reduced a little from 52% to 46.4%.

4.5.2 Maximized IDX-SAHP Evaluation

In this part, the IDX-SAHP system as per the MOO results is assessed, in-depth. In this context, the optimum parameters achieved by the MOO (provided in Table 6) were implemented to the initial IDX-SAHP and the maximized system was examined. As provided in Table 7, the largest COP was 8.4 in with the highest values for T_a (31 °C), I_T (570.552W/m^2), and MSHs (343 hours) throughout the year. Additionally, the smallest COP is 4.6 in December with the least values for I_T (307.8684 W/m^2), MSHs (161 hours), and T_a (5 °C) throughout the year. On the contrary, the largest CE is 77% in September with a small value for of I_T (524.7188 W/m^2), and almost high values for T_a (26 °C) and MSHs (320 hours) throughout the year. Furthermore, the least CE is 43% in February with a high value for I_T (391.942 W/m^2), and almost small values for T_a (6 °C) and MSHs (189 hours) throughout the year. To have $T_{W,o}$ of 5 0 ° C, the total working hour of the IDX-SAHP is 1037 hours throughout the year and ranges from 51 hours in July to 119 hours in December. In addition, $\dot{Q}_{cond}$ ranges from 100kWh in July to 323kWh in December. In the warm months, the working hour and $\dot{Q}_{cond}$ is smaller because $T_{W,i}$, T_a, I_T, and MSHs are larger and vice versa.

Consequently, although the CE of the maximized IDX-SAHP drops slightly, its COP is highly enhanced, resulting in a reduction in the total working hour up to 282 hours compared to the initial IDX-SAHP. In other words, the overall power use of the maximized IDX-SAHP largely lessens compared to the initial IDX-SAHP. Accordingly, the MOO presented a more optimal IDX-SAHP system compared to the SOOs.

5 Conclusions

This investigation proposed the numerical modeling of the indirect-expansion solar-assisted heat pump (IDX-SAHP), and the exergy-energy analysis and multiple-objective optimization (MOO) of the developed system were carried out. The performance of the proposed IDX-SAHP was completely assessed under the temperate climate of Iran. Next, the influences of design IDX-SAHP parameters such as T_a, I_T, $T_{W,o}$, ω, A_{cl}, k_p, N_{gl}, D_{cl}, L_{cond}, and δ were analyzed on the COP and CE using OPAT technique. Based on the results of OPAT, the IDX-SAHP performance was affected by the design parameters considerably so that the performance would be largely enhanced by selecting the appropriate IDX-SAHP components. Afterward, the exergy analysis of the IDX-SAHP system was conducted and the influence of T_a, I_T, A_{cl} and ω on exergy efficiency (η_{ex-sys}) and exergy destruction ($\dot{E\chi}_{des-sys}$) of the system were investigated. The exergy analysis showed that increasing the T_a leads to increase in η_{ex-sys} and reduction in $\dot{E\chi}_{des-sys}$ of the system. However, I_T had a more pronounced effect on exergy of the system compared to T_a and greatly reduced the η_{ex-sys} and increased the $\dot{E\chi}_{des-sys}$. Besides, increasing the A_{cl} reduced the η_{ex-sys} and increased $\dot{E\chi}_{des-sys}$ while increasing the ω increased the η_{ex-sys} and reduced the $\dot{E\chi}_{des-sys}$. Moreover, SOOs and MOO processes were implemented on the developed IDX-SAHP. The SOOs results indicated that the design of IDX-SAHP according to the COP-based optimization recommended better efficiency compared to the CE-based optimization. Also, the Pareto curve obtained by the MOO process depicted the COP and CE interactions. To achieve the final optimum layout of the IDX-SAHP, AHP MCDA method was integrated with MOO process. The achieved results demonstrated that the MOO approach yielded better

Table 7 Comparison of the maximized and initial IDX-SAHP

Month	Optimized IDX-SAH						Baseline IDX-SAHP		
	COP		CE%		Operating time (hour)		COP	CE%	Operating time (hour)
	Value	Diff%	Value	Diff%	Value	Diff (hour)	Value	Value	Value
January	4.9	+81	49	- 6	109	- 19	2.7	52	135
February	5.6	+51	43	- 16	112	- 18	3.7	51	138
March	6.5	+48	52	- 6	92	- 20	4.4	55	115
April	7.6	+49	61	- 2	75	– 22	5.1	62	96
May	7.9	+39	66	- 2	59	– 31	5.7	67	85
June	8.1	+35	71	- 3	52	– 35	6	73	80
July	8.4	+33	75	- 1	51	– 30	6.3	76	73
August	7.7	+45	73	- 1	72	– 23	5.3	80	94
September	6.9	+47	77	- 1	92	– 19	4.7	86	113
October	6.1	+45	74	- 1	97	– 18	4.2	75	118
November	5.2	+73	62	- 2	107	– 18	3	63	130
December	4.6	+92	54	- 1	119	– 16	2.4	58	142

comprehensive performance compared to the SOOs in such a way that although the CE of the maximized IDX-SAHP lessened a little from 52 to 47%, its COP is greatly enhanced from 3 to 7, resulting in reducing the total working hour up to 282 hours compared to the initial IDX-SAHP, and therefore, the overall power consumption of the maximized system largely lessened. This study declared the importance of SA, SOO, MOO, and MADA during the design of the IDX-SAHP to improve the performance and lessen the power use of the system via opting the best design parameters of the system. Our next research focuses on the environmental-economic evaluations of the maximized IDX-SAHP, construction of the maximized IDX-SAHP and performance analysis in different climate conditions of Iran, development and performance analysis of IDX-SAHP applying PV/T.

Data Availability All data generated or analyzed during this study are included in this published article (and its supplementary information files).

Declarations

Conflict of interest The authors have no conflict of interest.

References

1. Qiu, L.; He, L.; Lu, H.; Liang, D.: Systematic potential analysis on renewable energy centralized co-development at high altitude: a case study in Qinghai-Tibet plateau. Energy Convers. Manage. **267**, 115879 (2022). https://doi.org/10.1016/j.enconman.2022.115879
2. Zhong, C.; Zhou, Y.; Chen, J; Liu, Z.: DC-side synchronous active power control of two-stage photovoltaic generation for frequency support in Islanded microgrids. Engery Rep. **8**, 8361–8371 (2022). https://doi.org/10.1016/j.egyr.2022.06.030
3. Shi, G.; Aye, L.; Li, D.; Du, X.: Recent advances in direct expansion solar assisted heat pump systems: a review. Renew. Sustain. Energy Rev. **109**, 349–366 (2019)
4. Youssef, W., Experimental and computational study of indirect expansion solar assisted heat pump system with latent heat storage for domestic hot water production, Doctor of Philosophy (PhD) thesis, College of Engineering, Design, and Physical Sciences, Publisher: Brunel University London, 2017, 232, URI:http://bura.brunel.ac.uk/handle/2438/15263
5. Leonforte, F.; Miglioli, A.; Pero, C.D.; Aste, N.; Cristiani, N.; Croci, L.; Besagni, G.: Design and performance monitoring of a novel photovoltaic-thermal solar-assisted heat pump system for residential applications. Appl. Therm. Eng. **210**, 118304 (2022)
6. Cao, Y.; Mihardjo, L.W.W.; Parikhani, T., Thermal performance, parametric analysis, and multi-objective optimization of a direct-expansion solar-assisted heat pump water heater using NSGA-II and decision makings, Applied Thermal Engineering, Volume **181**, 25 115892 (2020)
7. Song, Z.; Jie Ji, J.; Cai, J.; Zhao, B.; Li, Z.: Investigation on a direct-expansion solar-assisted heat pump with a novel hybrid compound parabolic concentrator/photovoltaic/fin evaporator. Appl. Energy **299**, 117279 (2021)
8. Mohanraj, M.; Karthick, L.; Dhivagar, R.: Performance and economic analysis of a heat pump water heater assisted regenerative solar still using latent heat storage. Appl. Therm. Eng. **196**, 117263 (2021)
9. Duarte, W.M.; Rabelo, S.N.; Paulino, T.F.; Pabón, J.G.; Machado, L.: Experimental performance analysis of a CO_2 direct-expansion solar assisted heat pump water heater. Int. J. Refrig **125**, 52–63 (2021)
10. Singh, A.; Sarkar, J.; Sahoo, R.R.: Experimentation on solar-assisted heat pump dryer: thermodynamic, economic and exergoeconomic examinations. Sol. Energy **208**, 150–159 (2020)
11. Kong, X.; Yang, Y.; Zhang, M.; Li, Y.; Li, J.: Experimental investigation on a direct-expansion solar-assisted heat pump water heater using R290 with micro-channel heat transfer technology during the winter period. Int. J. Refrig **113**, 38–48 (2020)

12. Belmonte, J.F., Díaz-Heras, M., Almendros-Ibáñez, J.A., Cabeza, Luisa F., Simulated performance of a solar-assisted heat pump system including a phase-change storage tank for residential heating applications: a case study in Madrid, Spain, Journal of Energy Storage, 103615 (2021)
13. Sezen, K.; Tuncer, A.D.; Akyuz, A.O.; Gungor, A.: Effects of ambient conditions on solar assisted heat pump systems: a review. Sci. Total Environ. **778**, 146362 (2021)
14. Song, Z.; Ji, J.; Cai, J.; Li, Z.; Yu, B.: The performance comparison of the direct-expansion solar assisted heat pumps with three different PV evaporators. Energy Convers. Manage. **213**, 112781 (2020)
15. Singh, A.; Sarkar, J.; Sahoo, R.R.: Experimental energy, exergy, economic and exergoeconomic analyses of batch-type solar-assisted heat pump dryer. Renewable Energy **156**, 1107–1116 (2020)
16. Simonetti, R.; Moretti, L.; Molinaroli, L.; Manzolini, G.: Energetic and economic optimization of the yearly performance of three different solar assisted heat pump systems using a mixed integer linear programming algorithm. Energy Convers. Manage. **206**, 112446 (2020)
17. Chen, J.; Zhang, G.; Wang, D.: Experimental investigation on the dynamic characteristic of the direct expansion solar assisted ejector-compression heat pump cycle for water heater. Appl. Therm. Eng. **195**, 117255 (2021)
18. Yang, L.W., Hua, N., Pu, J.H., Y Xia, Y., Zhou, W.B., Xu, R.J., Yang, T., Belyayev, Y., Wang, H.S., Analysis of operation performance of three indirect expansion solar assisted air source heat pumps for domestic heating, Energy Conversion and Management, **252**, 115061 (2022)
19. Li, Y.H.; Mao, W.C.: Taguchi optimization of solar thermal and heat pump combisystems under five distinct climatic conditions. Appl. Therm. Eng. **133**, 283–297 (2018)
20. Zhou, J.; Zhu, Z.; Zhao, X.; Yuan, Y.; Fan, Y.; Myers, S.: Theoretical and experimental study of a novel solar indirect-expansion heat pump system employing mini channel PV/T and thermal panels. Renewable Energy **151**, 674–686 (2020)
21. Kim, T.; Choi, B.I.; Han, Y.S.; Do, K.H.: A comparative investigation of solar-assisted heat pumps with solar thermal collectors for a hot water supply system. Energy Conv, Manag **172**, 472–484 (2018)
22. Huan, C.; Wang, F.; Li, S.; Zhao, Y.; Liu, L.; Wang, Z.; Ji, C.: A performance comparison of serial and parallel solar-assisted heat pump heating systems in Xi'an. China. Energy Sci. Eng. **7**, 1379–1393 (2019)
23. Ma, J.; Fung, A.S.; Brands, M.; Juan, N.; Abul Moyeed, O.M.: Performance analysis of indirect-expansion solar assisted heat pump using CO2 as refrigerant for space heating in cold climate. Sol. Energy **208**, 195–205 (2020)
24. Singh, A.; Sarkar, J.; Sahoo, R.R.: Experimental performance analysis of novel indirect-expansion solar infrared assisted heat pump dryer for agricultural products. Sol. Energy **206**, 907–917 (2020)
25. Liu, Y.; Zhang, H.; Chen, H.: Experimental study of an indirect-expansion heat pump system based on solar low-concentrating photovoltaic/thermal collectors. Renewable Energy **157**, 718–730 (2020)
26. Youssef, W.; Ge, Y.; Tassou, S.A.: Indirect expansion solar assisted heat pump system for hot water production with latent heat storage and applicable control strategy. Energy Procedia **123**, 180–187 (2017)
27. Bridgeman, A., Experimental analysis of an indirect solar assisted Heat pump for domestic water heating, Master of Applied Science thesis, Department of Mechanical and Materials Engineering, Queen's University, Kingston, Ontario, Canada, 2010, 172 Pages. https://qspace.library.queensu.ca/bitstream/handle/1974/6129/Bridgeman_Andrew_G_201009_MASc.pdf?sequence=3
28. Freeman, T.L.; Mitchell, J.W.; Audit, T.E.: Performance of combined solar-heat pump systems. Sol. Energy **22**(2), 125–135 (1979)
29. Oztop, H.F.; Bayrak, F.; Hepbasli, A.: Energetic and exergetic aspects of solar air heating (solar collector) systems. Renew. Sustain. Energy Rev. **21**, 59–83 (2013)
30. Bayrak, F.; Oztop, H.F.; Hepbasli, A.: Energy and exergy analyses of porous baffles inserted solar air heaters for building applications. Energy Build. **57**, 338–345 (2013)
31. Zhang, W.; Qi, H.; Yu, Z.; He, M.; Ren, Y.; Li, Y.: Optimization configuration of selective solar absorber using multi-island genetic algorithm. Sol. Energy **224**, 947–955 (2021)
32. Kong, X.Q.; Zhang, D.; Li, Y.; Yang, Q.M.: Thermal performance analysis of a direct-expansion solar-assisted heat pump water heater. Energy **36**(12), 6830–6838 (2011)
33. Bergman, T.L., Lavine, A.S., Incropera, F.P., DeWitt, D.P.: Fundamentals of Heat and Mass Transfer, 8th Edition, ISBN: 978-1-119-53734-2, 992 (2019)
34. Cleland, A.C.: Polynomial curve-fits for refrigerant thermodynamic properties: extension to include R134a. Int. J. Refrig **17**(4), 245–249 (1994)
35. Klein, S.A., Alvarado, F.L., EES- engineering equation solver, commercial academic pro, Version 8.400, F-Chart Software, 4406 Fox Bluff Rd Middleton, WI, 53562, (1997)
36. Yu, D.; Wu, J.; Wang, W.; Gu, B.: Optimal performance of hybrid energy system in the presence of electrical and heat storage systems under uncertainties using stochastic p-robust optimization technique. Sustain. Cities Soc. (2022). https://doi.org/10.1016/j.scs.2022.103935
37. Zhang, L.; Gao, T.; Cai, G.; Hai, K.L.: Research on electric vehicle charging safety warning model based on back propagation neural network optimized by improved gray wolf algorithm. J Energy Storage. **49**, 104092 (2022). https://doi.org/10.1016/j.est.2022.104092
38. Chen, H.; Fu, Q.; Liao, Q.; Zhu, X.; Shah, A.: Applying artificial neural network to predict the viscosity of microalgae slurry in hydrothermal hydrolysis process. Energy and AI **4**, 100053 (2021)
39. Mou, J.; Duan, P.; Gao, L.; Liu, X.; Li, J.: An effective hybrid collaborative algorithm for energy-efficient distributed permutation flow-shop inverse scheduling. Futur. Gener. Comput. Syst. **128**, 521–537 (2022). https://doi.org/10.1016/j.future.2021.10.003
40. Petela, R.: Exergy of undiluted thermal radiation. Sol. Energy **74**(6), 469–488 (2003)
41. Zhang, L.; Zhang, H.; Cai, G.: The multiclass fault diagnosis of wind turbine bearing based on multisource signal fusion and deep learning generative model. IEEE Trans. Instrum. Meas. **71**, 1–12 (2022). https://doi.org/10.1109/TIM.2022.3178483
42. Li, P.; Li, Y.; Gao, R.; Xu, C.; Shang, Y.: New exploration on bifurcation in fractional-order genetic regulatory networks incorporating both type delays. Eur. Phys. J. Plus (2022). https://doi.org/10.1140/epjp/s13360-022-02726-3
43. Yan, A.; Chen, Y.; Hu, Y.; Zhou, J.; Ni, T.; Cui, J.; Girard, P.; Wen, X.: Novel speed-and-power-optimized SRAM cell designs with enhanced self-recoverability from single- and double-node upsets. IEEE Trans. Circuits Syst. I Regul. Pap. **67**(12), 4684–4695 (2020). https://doi.org/10.1109/TCSI.2020.3018328
44. Yan, A.; Xu, Z.; Feng, X.; Cui, J.; Chen, Z.; Ni, T.; Huang, Z.; Girard, P.; Wen, X.: Novel quadruple-node-upset-tolerant latch designs with optimized overhead for reliable computing in harsh radiation environments. IEEE Trans. Emerg. Top. Comput. **10**(1), 404–413 (2022). https://doi.org/10.1109/TETC.2020.3025584
45. Delgarm, N.; Sajadi, B.; Delgarm, S.; Kowsary, F.: A novel approach for the simulation-based optimization of the buildings energy consumption using NSGA-II: Case study in Iran. Energy Build. **127**(1), 552–560 (2016)
46. Qiu, L.; He, L.; Lu, H.; Liang, D.: Pumped hydropower storage potential and its contribution to hybrid renewable energy

co-development: A case study in the Qinghai-Tibet Plateau. J. Energ. Storage **51**:104447 (2022). https://doi.org/10.1016/j.est.2022.104447
47. Lv, Z.; Guo, J.; Lv, H.: Safety poka yoke in zero-defect manufacturing based on digital twins. IEEE Trans. Industr. Inf. (2022). https://doi.org/10.1109/TII.2021.3139897
48. Zhu, B.; Zhong, Q.; Chen, Y.; Liao, S.; Li, Z.; Shi, K.; Sotdoi, M.A.: A novel reconstruction method for temperature distribution measurement based on ultrasonic tomography. IEEE Trans. Ultrason. Ferroelectr. Freq. Control **69**(7), 2352–2370 (2022). https://doi.org/10.1109/TUFFC.2022.3177469
49. Delgarm, N.; Sajadi, B.; Delgarm, S.: Multi-objective optimization of building energy performance and indoor thermal comfort: a new method using artificial bee colony (ABC). Energy and Buildings **131**, 42–53 (2016)
50. Yu, D.; Ma, Z.; Wang, R.; Pan, W-T.: Efficient smart grid load balancing via fog and cloud computing. Math. Probl. Eng. **2022**, 1–11. https://doi.org/10.1155/2022/3151249
51. Lu, C.; Liu, Q.; Zhang, B.; Yin, L.: A Pareto-based hybrid iterated greedy algorithm for energy-efficient scheduling of distributed hybrid flowshop. Expert Syst. Appl. **204**, 117555 (2022). https://doi.org/10.1016/j.eswa.2022.117555
52. Delgarm, N., Sajadi, Delgarm, S., Kowsary, F. (2016) Multi-objective optimization of the building energy performance: A simulation-based approach by means of particle swarm optimization (PSO), Appl. Energy, 170: 293-303
53. Zhang, L.; Zheng, H.; Cai, G.; Zhang, Z.; Wang, Z.; Koh.: Power-frequency oscillation suppression algorithm for AC microgrid with multiple virtual synchronous generators based on fuzzy inference system. IET Renew. Power Gener. **16**(8), 1589–1601. https://doi.org/10.1049/rpg2.12461
54. Cai, T.; Yu, D.; Liu, H.; Gao, F.: Computational analysis of variational inequalities using mean extra-gradient approach. Mathematics **10**(13), 2318 (2022). https://doi.org/10.3390/math10132318
55. Ayadi, O.; Felfel, H.; Masmoudi, F.: Analytic hierarchy process-based approach for selecting a Pareto-optimal solution of a multi-objective, multi-site supply-chain planning problem. Eng. Optim. (2016). https://doi.org/10.1080/0305215X.2016.1242913
56. Saaty, T.L.: The Analytic Hierarchy Process. McGraw-Hill, New York (1980)
57. Ioan Sarbu Calin Sebarchievici, "Solar Heating and Cooling Systems", Imprint: Academic Press, ISBN: 9780128116630, Published Date: p. 432 (2016)
58. Jean-Christophe, H., "Solar and Heat Pump Systems for Residential Buildings", ISBN: 978-3-433-03040-0, p. 274
59. Zhao, X., Ma, X.: Advanced Energy Efficiency Technologies for Solar Heating, Cooling and Power Generation (Green Energy and Technology), Publisher : Springer; 1st ed. 2019 edition (July 22, 2019), ISBN-10: 3030172821, p. 550
60. Baker, E.: Solar Heating and Cooling Systems: Design for Australian Conditions null, Publisher: Australian Natl Univ Pr (January 1, 1985), ISBN-10: 0080298524, p. 332
61. Nasouri, M.; Delgarm, N.: Bushehr Nuclear Power Plants (BNPPs) and the perspective of sustainable energy development in Iran. Prog. Nucl. Energy **147**, 104179 (2022)
62. Delgarm, N., Sepanloo, K., Haghighi Shad, A., Masti, D., Design and development of a comprehensive program for the assessment and analysis of environmental effects due to the release of radioactive materials from the stack of nuclear installations: a case study in Bushehr nuclear power plant, Appl. Radiation Isotopes, **166**, 109383 (2020)
63. Zhou, H.; Xu, C.; Lu, C.; Jiang, X.; Zhang, Z.; Wang, J.; Xiao, X.; Xin, M.; Wang, L.: Investigation of transient magnetoelectric response of magnetostrictive/piezoelectric composite applicable for lightning current sensing. Sens. Actuators A Phys. **329**, 112789 (2021). https://doi.org/10.1016/j.sna.2021.112789
64. Huang, S.; Huang, M.; Lyu, Y.: Seismic performance analysis of a wind turbine with a monopile foundation affected by sea ice based on a simple numerical method. Eng. Appl. Comput. Fluid Mech. **15**(1), 1113–1133 (2021). https://doi.org/10.1080/19942060.2021.1939790
65. Shang, L.; Dong, X.; Liu, C.; He, W.: Modelling and analysis of electromagnetic time scale voltage variation affected by power electronic interfaced voltage regulatory devices. IEEE Trans. Power Syst. **37**(2), 1102–1112 (2022). https://doi.org/10.1109/TPWRS.2021.3100606
66. Tehran Meteorological Station Report, Data Processing Center, Iranian Meteorological Organization, Iran (2019–2020)
67. Delgarm, N., Sajadi, B., Azarbad, Kh., Delgarm, S., Sensitivity analysis of building energy performance: a simulation-based approach using OFAT and variance-based sensitivity analysis methods, Journal of Building Engineering, 15, pp. 181–193 (2018)
68. Shen, Z.; Wang, F.; Wang, Z.; Li, J.: A critical review of plant-based insulating fluids for transformer: 30-year development. Renew. Sustain. Energ. Rev. **141**, 110783 (2021). https://doi.org/10.1016/j.rser.2021.110783
69. Lu, C.; Zhu, H.; Li, L.; Yang, A.; Xu, C.; Ou, Z.; Wang, J.; Wang, X.; Tian, F.: Split-core magnetoelectric current sensor and wireless current measurement application. Measurement **188**, 110527 (2022). https://doi.org/10.1016/j.measurement.2021.110527
70. Lu, c.; Zhu, R.; Yu, F.; Jiang, X.; Liu, Z.; Dong, L.; Hua, Q.; Ou, Z,; et al.: Gear rotational speed sensor based on FeCoSiB/Pb(Zr,Ti)O3 magnetoelectric composite. Measurement **198**,108409 (2021). https://doi.org/10.1016/j.measurement.2020.108409
71. Cai, J.; Ji, J.; Wang, Y.; Huang, W.: Numerical simulation and experimental validation of indirect expansion solar-assisted multifunctional heat pump. Renew Energy **93**, 280–290 (2016)
72. Meena, C.S., Raj, Binju P., Saini, L., Agarwal, N., Ghosh, A.: Performance optimization of solar-assisted heat pump system for water heating applications, Energies, 14(12), 3534. https://doi.org/10.3390/en14123534 (2021)
73. Wang, Q.; Liu, Y.Q.; Liang, G.F.; Li, J.R.; Sun, S.F.; Chen, G.M.: Development and experimental validation of a novel indirect-expansion solar-assisted multifunctional heat pump. Energy Build. **43**, 300–304 (2011)
74. Zhang, D.; Wu, Q.B.; Li, J.P.; Kong, X.Q.: Effects of refrigerant charge and structural parameters on the performance of a direct-expansion solar-assisted heat pump system. Appl. Therm. Eng. **73**(1), 522–528 (2014)